



# UNIVERSITÀ DI PISA

Dipartimento di Fisica E. Fermi  
Corso di Laurea Magistrale in Fisica

## Study of monolithic CMOS pixel sensors in the Belle II experiment upgrade

Candidato:  
**Mara Stefania Caló**

Relatore:  
**Prof. Francesco Forti**

Correlatore:  
**Dott. Nome Cognome**

Anno accademico 2022/2023

# Contents

<b>Introduction</b>	<b>3</b>
<b>1 TJ-Monopix 2 characterization</b>	<b>5</b>
1.1 Matrix and flavors . . . . .	6
1.1.1 Flavors . . . . .	6
1.1.2 Pixel design . . . . .	7
1.1.2.1 Improved front-end circuit design . . . . .	7
1.2 Threshold and noise . . . . .	9
1.2.1 Injection circuit . . . . .	9
1.2.2 S-Curve method . . . . .	9
1.2.2.1 Normal FE . . . . .	10
1.2.2.2 Cascode FE . . . . .	10
1.2.2.3 HV-Cascode FE . . . . .	11
1.2.2.4 HV-Normal FE . . . . .	12
1.2.2.5 Summary Table . . . . .	14
1.2.3 Threshold dispersion and tuning . . . . .	15
1.2.3.1 First results from threshold tuning . . . . .	16
1.3 ToT calibration with internal injection . . . . .	17
1.3.1 Time Over Threshold (TOT) curves and fit . . . . .	19
1.4 Response to radioactive source and absolute calibration . . . . .	19
1.4.1 $^{55}\text{Fe}$ . . . . .	21
1.4.2 $^{241}\text{Am}$ . . . . .	21

1.4.3	$^{109}\text{Cd}$	21
1.4.4	Injection capacitance calibration	22
1.4.5	Check on calibration curve ToT vs $Q_{inj}$ with radioactive sources	24
1.5	Operation with low threshold	25
1.5.1	Register optimization	26
1.5.2	Comparison between data and simulation	27
1.5.2.1	some nice picture of the optimized thr and tuning	28
1.6	Cross talk issue and mitigation	29
1.6.1	Hot pixel issue	29
1.6.2	Hot pixel strategy (study)	31
1.6.3	Cross-talk (Results)	32
1.6.4	Mitigation	34
1.6.4.1	Final results?	36
1.7	Test Beam results	36
1.7.1	Experimental apparatus and DUTs	37
1.7.2	Hit detection efficiency measurements	38
<b>2</b>	<b>Conclusions</b>	<b>41</b>

# Introduction

Belle II is a particle physics experiment located at the KEK laboratory in Tsukuba (Japan). The detector is a general-purpose spectrometer to study electron-positron collisions produced by the SuperKEKB accelerator, a second generation flavor-factory which operates at the luminosity frontier, holding the world record of instantaneous luminosity with  $L_{peak} = 4.7 \times 10^{34} \text{ cm}^{-2} \text{ s}^{-1}$ .

SuperKEKB is the upgrade of the preceding facility KEKB (operational from 1998 to 2016) and it consists in a 3 km-circumference asymmetric accelerator which collides electrons and positrons beams at a center-of-mass energy near the  $\Upsilon(4S)$  resonance ( $\sqrt{s} = 10.58 \text{ GeV}$ ). It started its data taking in March 2019.

In the next decade, the collider aims to collect an unrivaled dataset of  $50 \text{ ab}^{-1}$  (x50 Belle dataset, x100 BaBar dataset) and to reach a peak luminosity of  $6 \times 10^{35} \text{ cm}^{-2} \text{ s}^{-1}$ . This will allow to study the charge-parity violation in B mesons system with more precision and to search for new hints of physics beyond the Standard Model.

To achieve these challenging targets, it will be necessary a significant upgrade of the accelerator and its main components (like the injection system and the equipment nearby the interaction region), probably requiring the installation of a new vertex detector. As a matter of fact, to the increase in luminosity corresponds not only large data collected and greater possibility to study rare processes, but also higher doses of radiation and larger backgrounds, which could undermine the integrity and the operation of the Belle II detector. In particular the subdetectors which are closest to the beam pipe are those more exposed to severe conditions, like the vertex detector (VXD), composed of the inner pixel detector (PXD, made of layers of pixels) and the outermost silicon vertex detector (SVD, made of layers of strips). They allow the reconstruction of charged particle tracks and of decay vertices with high performance. Recent studies have shown that the current detector could operate efficiently up to a luminosity of  $L_{inst} = 2 \times 10^{35} \text{ cm}^{-2} \text{ s}^{-1}$ , but safety margins are not large. Consequently, in this context, different upgrade projects have been proposed, which intend to design a new vertex detector, making it more resistant even in harsher working conditions, while the luminosity will be gradually increased.

This work focuses especially on the VerTeX Detector (VTX) proposal (the one chosen for the upgrade), replacing the whole VXD with five layers of fully pixelated sensors based on the CMOS Depleted Monolithic Active Pixel Sensor (DMPAS) technology.

The good results achieved by the ALICE experiment (LHC, CERN), which employed the same technology, have suggested this solution which has proven to be reliable and the current developments, aimed at making the chips much faster than in ALICE, are promising in maintaining low occupancy, despite the worse expected background environment, and good radiation hardness even after irradiation.

In order to fulfill the physics requirements of Belle II experiment, a new silicon sensor is being designed, called OBELIX, exploiting the 180 nm TowerJazz Semiconductor process. Developments will ensure a faster, lighter and highly granular chip, reducing the material budget and improving tracks and vertices reconstruction.

OBELIX planning is based on studies done on previous prototypes, among which TJ-Monopix 2, whose characterization is the main topic of this thesis. Laboratory and beam tests have been conducted and are still in progress, in order to study the efficiency of the chip before and after irradiation, its power consumption, and to fully characterize its electrical characteristics. In particular, we have characterized the response of the pixel matrix, extracting important results that have allowed to interpret data taken during the Test Beam at Desy (July 2022), and that are being used in the design of the OBELIX chip. In more details, the threshold distributions for all the different types of front-end circuits implemented in the matrix have been studied, together with their dispersion and noise distributions. The calibration of the Time Over Threshold curves (which is a time width signal processing method used in this prototype) has been done by internal injection tests. The absolute calibration of the whole matrix has been achieved, employing a  $^{55}\text{Fe}$  radioactive source. Other radioactive sources have been used too, in order to check the trend of the ToT curves for charge values not accessible by internal injection. Additionally, different register settings have been examined in the interest of operating the matrix at low threshold, that is crucial to keep high efficiency even after irradiation. For this reason, several tests have been conducted to tune the threshold, in order to reduce the dispersion and make the threshold on the matrix as uniform as possible. During this investigation, a cross-talk issue has been discovered and therefore studied to understand its causes and possible solutions to mitigate this effect.

?? briefly introduces some of the open questions in the Standard Model, in order to depict the background of the Belle II physics program. Then a short description of the SuperKEKB accelerator and Belle II detector is given, too.

?? presents the fundamental reasons behind the choice of an upgrade. The primary sources of the experiment background are summarized, to understand the limitation of the detector and the accelerator, for increasingly higher luminosity values. Eventually a summary of the four main upgrade proposals for the vertex detector is presented, which are distinguished by the different type of sensors employed: Depleted Field Effect Transistor (DEPFET), Thin and Fine-Pitch SVD, Silicon On Insulator (SOI) and CMOS Monolithic Active Pixels Sensors.

?? describes the principles underlying the operation of semiconductor detectors and some different type of sensors which use this technology, like the hybrid and monolithic pixel sensors. In particular the CMOS Monolithic Active Pixel Sensors technology is presented, on which the entire developments of the OBELIX chip is based. In the end, the history of the developments that led to the TJ-Monopix chip series is retraced, in order to better understand the main features of the last one, TJ-Monopix 2, which represents the starting point for OBELIX design, and whose characterization is the work of this thesis.

?? examines in depth the VerTeX detector (VTX) upgrade program, which involves the CMOS Monolithic Active Pixel Sensors as fundamental components of the five layers of the final vertex detector. Studies and simulations are ongoing to test the performance, and some of them are shown here. The specifications and the implementation of the new chip (OBELIX) under design for this proposal are described. The innovative sensor has to fulfill the requirements of Belle II experiment, even in extreme environment due to higher doses of radiation and backgrounds.

Chapter 1 lastly shows the results obtained from laboratory measurements and tests conducted on the TJ-Monopix 2 chip. The response of the matrix has been studied in different working conditions, in order to analyze the behaviour at high and low threshold. The absolute calibration of the all front-end circuits implemented in the chip, has been done too. Moreover a cross-talk issue have been discovered and analyzed, in order to understand its causes and a possible mitigation of this effect since it prevented from using the matrix at low threshold.

# 1. TJ-Monopix 2 characterization

In the previous chapter we have seen the fundamental steps that had lead to the development of the CMOS MAPS sensors technology and the history of their many different prototypes. Here we will go through the main features of TJ-Monopix 2 designed to address efficiency degradation after irradiation, one of the main issues of its predecessor TJ-Monopix 1. The characterization of the chip is crucial in the VTX upgrade program and in the design of the next OBELIX chip.

The chip W14R12, which is one of the sensors tested during the first Test Beam campaign in Desy (July 2022) has been fully characterized in Pisa and in particular several aspects have been analyzed, among which:

1. TOT calibration by internal charge injection;
2. characterization with radioactive sources and absolute calibration;
3. systematic study of different registers' settings in order to operate the chip at low thresholds;
4. investigation of an important issue with cross-talk, due to digital signal from the readout, discovered trying to operate the matrix at low threshold (below  $250 e^-$ ).

This detailed characterization returned crucial results (1, 2) for the Test Beam data reconstruction and the simulations of the upgraded VTX detector with CMOS MAPS devices. Furthermore the optimization of the registers to reduce the operating threshold was very useful for the preparation of the next TB (July 2023) campaign with irradiated sensors.

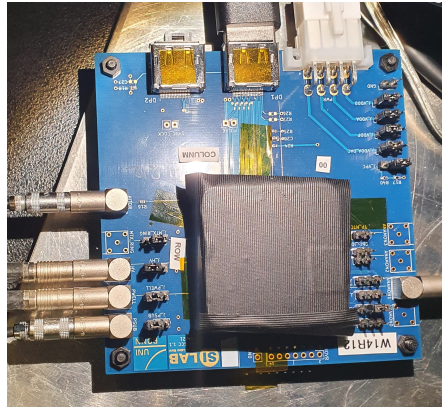


Figure 1.1: The W14R12 chip tested during the Test Beam in Desy.

## 1.1 Matrix and flavors

Tj-Monopix 2 is the next generation small collection electrode DMAPS prototype in TowerJazz 180 nm. The need to create a sensor capable to mantain high efficiency even after irradiation, required improvements compared to Tj-Monopix 1 in two important fields: a lower operating threshold to keep a good efficiency with the reduced charge collected after irradiation and smaller pixel pitch to increase charge collection efficiency all over its area, expecially in the corners.

To achieve these goals, a different in-pixel front-end circuit was implemented and a lot of efforts have been focused on optimizing pixel layout in order to reduce its size, which has been decreased from  $36 \times 40 \mu\text{m}^2$  in TJ-Monopix1 to  $33.04 \times 33.04 \mu\text{m}^2$  (pixel *pitch*). As a matter of fact we have seen (REFERENCE) that pixel dimensions are critical to accomplish faster charge collection across all active area, increasing the lateral electric field. For this reason it was necessary a special effort to design and create a smaller pixel but still adequate to embody the full digital readout. All of this required to work at the technology density limit and also to study for further modifications at the circuit design.

In order to operate with a lower threshold TJ-Monopix2 incorporates an improved front-end circuit that reduces the noise by  $\approx 40\%$  and the threshold dispersion by about 80-90% with respect to TJ-Monopix1. Furthermore, in-pixel threshold tuning has been integrated in order to achieve a more uniform threshold distribution across the pixel matrix, particularly after irradiation. [Pixel masking is also improved by employing individual in-pixel configuration memory that eliminates the issue of unintentionally masked ghost pixels and allows for a more efficient configuration of the pixel matrix and reduced noise hit rate.] As a result of these improvements, the operating threshold was expected to be at  $\approx 100 e^-$ , three times lower than in TJ-Monopix1.

### 1.1.1 Flavors

The prototype is a  $2 \times 2 \text{ cm}^2$  pixel matrix which consists of  $512 \times 512$  pixels and all of them are designed with a reduced deep p-well geometry (RDPW) because, as it was demonstrated during the testing of TJ-Monopix1, this type of arrangement has superior charge collection properties compared to full deep p-well coverage (FDPW) (Figure 1.2). The total active area of the matrix is approximately  $286 \text{ mm}^2$  and it is  $300 \mu\text{m}$  thick.

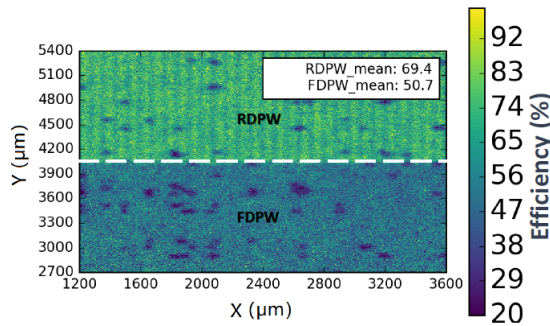


Figure 1.2: Detection efficiency map of a TJ-Monopix1 chip with  $25 \mu\text{m}$  p-epitaxial layer that has been irradiated to  $10^{15} \text{ n}_{eq}/\text{cm}^2$  NIEL.

As we can see in Figure 1.3, the matrix is divided in four sectors, named **flavors** that imple-

ment different variation of the front-end circuit. In the first two flavors the collection electrode is DC-coupled directly with the readout electronics, the continuous baseline reset is implemented by a forward bias diode and they differ for the pre-amplifier circuit design. The second flavor indeed, named **Cascode FE**, includes an extra-cascode transistor that increases the pre-amplifier gain which in turn leads to a 50% reduction of the threshold dispersion compared to the first flavor, the **Normal FE**. The other two flavors consist of AC-coupled pixels (through a metal-oxide-metal MOM capacitor) and in particular, the **HV-Cascode FE** also incorporates the aforementioned pre-amplifier variation. AC-coupling allows to apply an high positive bias voltage (HV stands for High Voltage) to the collection electrode which potentially enlarges the depleted region, but at the same time it also causes signal losses mainly due to the additional parasitic capacitance introduced at the sensitive input node.

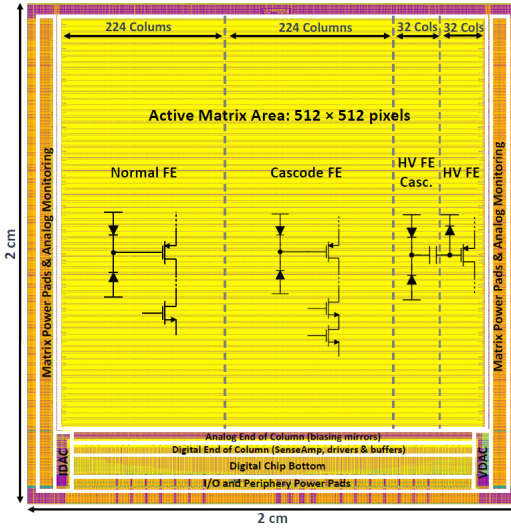


Figure 1.3: The layout of the TJ-Monopix2 prototype divided in four different flavors: **Normal**, **Cascode**, **HV-Cascode** and **HV FE**.

### 1.1.2 Pixel design

The  $2 \times 2$  pixel core layout, shown in Figure 1.4, is fully optimized and is designed in order to share as much features as possible between the four pixels. The analog area incorporates the front-end circuit, the 3-bit threshold tuning DAC and the pixel configuration registers. The digital region is composed by the 7-bit LE and TE memory (14 SRAM cells per pixel), the 10 bit address ROM (2 bit for the pixel position inside the core and 8 for the group address) and the readout control logic.

#### 1.1.2.1 Improved front-end circuit design

As we have seen above, there are two variations of the front-end circuit (Figure 1.5), such as *normal* and *cascode* type. The latter in particular includes an extra cascode transistor which increases the pre-amplifier gain and consequently reduces the threshold dispersion. Moreover in TJ-Monopix2 it was preferred to incorporate a simple diode to reset the input node

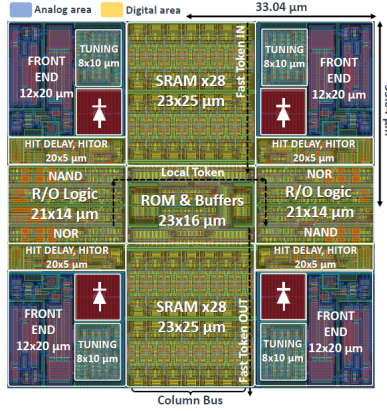


Figure 1.4: Layout of a TJ-Monopix2  $2 \times 2$  pixel core. In blue the analog area and in yellow the digital one.

instead of a PMOS transistor, which was the technology implemented in TJ-Monopix1. A side effect of this choice is that the relationship between charge injected and the ToT of the detected signal is not linear anymore, because the diode is a not linear element and its discharge rate also depends on the collected charge. Indeed in the following analysis it was necessary to fit the ToT trend with a more complex function. But at the same time, the advantages are its simplicity ( $p^+$  diffusion within the n-well collection electrode) and also the fact that it allows to increase radiation tolerance to TID effects, which was one of the key working area in the upgrade of the sensor.

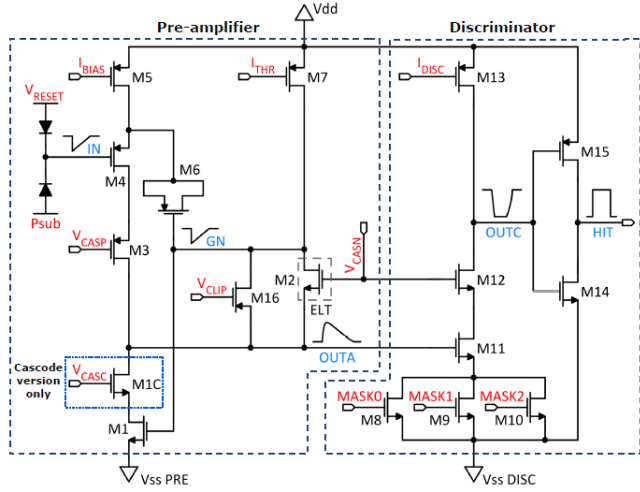


Figure 1.5: Schematic of the improved front-end circuit and its variation (extra-cascode transistor) in TJ-Monopix 2.

In the last two AC-coupled flavors are implemented the same improvements, but here the different coupling provokes an important loss in the collected charge, as verified during the testing phase of TJ-Monopix 1 (50% losses), due at most to additional parasitic capacitances. Thus a

lot of efforts have been made to improve this aspect, working on the coupling capacitor values. A signal loss of 41.5% has been reached in Tj-Monopix 2, which is a relevant enhancement with respect to its predecessor.

## 1.2 Threshold and noise

**Explain here what are NOISE, THR and THR dispersion, and why they are important figure of merit for the operation.**

see for example Eleonora's thesis sec 4.1.1.

To measure the threshold and noise of the whole matrix, the response of each pixel has been characterized by means of the internal charge injection.

### 1.2.1 Injection circuit

The hit injection circuit included in TJ-Monopix2 is similar to the one of TJ-Monopix1. It allows to produce artificial hits on each pixel through an injection capacitance  $C_{inj}$  connected at the collection electrode. The injected charge is proportional to the injection voltage pulse amplitude:  $Q_{inj} = C_{inj} \cdot \Delta V_{inj}$ . The injection pulse is set by two registers "V<sub>L</sub>" and "V<sub>H</sub>", with  $\Delta V_{inj} = V_H - V_L$ , and the minimum injection step is given by the DAC resolution, with the *Least Significant Bit* (LSB) = 7.03 mV.

The injected signal is then often expressed in DAC units  $Q_{inj}(DAC)$  and can be converted to electrons using the design value of the injection capacitance  $C_{inj} = 230 \text{ aF}$ , the same for the all the FEs implemented. The nominal conversion factor  $K$  from DAC to e- corresponds to the injected charge given by a voltage step of 1 DAC:

$$K = C_{inj} \cdot LSB = \frac{230 \text{ aF}}{q_{e^-}} \cdot 7.03 \frac{\text{mV}}{DAC} = 1.4375 \frac{e^-}{mV} \cdot 7.03 \frac{mV}{DAC} \approx 10.1 \frac{e^-}{DAC} \quad (1.1)$$

An absolute calibration of the conversion factor  $K$  (i.e. of the injection capacitance  $C_{inj}$ ) has been also performed using radioactive sources, as explained in section 1.4, obtaining results in agreement within 10% from the design value.

The conversion factor of equation 1.1 has been used to convert the information of the injected charge from DAC unit to electrons unit, useful for further analysis.

The response of each pixel to internal injection has been measured to extract their threshold and noise with the *s-curve method* explained in next section. The four flavors have been separately analyzed to be able to study their main differences concerning their performance and features.

### 1.2.2 S-Curve method

The response of the pixels is measured injecting different amounts of charge into the pixel a given number of times and recording the amount of registered hits (i.e. the signal is above the discriminator threshold). For each value of the input signal we measure the occupancy, or hit probability, as the fraction of events where the pixel has registered an hit. This occupancy has the typical S-curve shape shown in Figure 1.6 as an example.

As the injected signal passes the discriminator threshold the pixel starts to register some hits, finally reaching a plateau corresponding to the total number of injected events. This behaviour produces a step function smeared by the fluctuation on the input signal due to the noise. The threshold of the pixel corresponds to the injected signal that gives 50% occupancy, while the noise influences the slope of the S-curve.

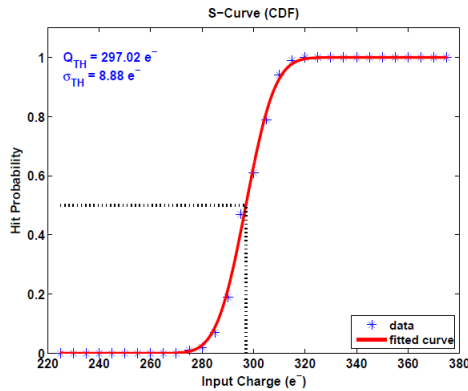


Figure 1.6: An example of the S-Curve fitted by the CDF to evaluate threshold and noise.

Assuming a gaussian noise distribution the S-curve can be fit with the *Cumulative Distribution Function (CDF)*:

$$CDF(x, \mu, \sigma) = \frac{1}{2} \cdot \left( 1 + erf\left(\frac{x - \mu}{\sigma\sqrt{2}}\right) \right) \quad (1.2)$$

where "erf" is the Gauss error function,  $x$  is the injected signal,  $\mu$  and  $\sigma$  are respectively the threshold and noise of the pixel.

This method allows to measure the noise and the threshold of all pixels and also the threshold dispersion across an entire FE.

In the following sections are reported the results of this study for the four flavors of matrix. The injected signal was varied, with the corresponding voltage injection registers "**VL, VH**" , from 0 to 140 equation 1.1 .

### 1.2.2.1 Normal FE

The first flavor of the matrix is the **Normal FE**, which consist of 512 rows and 224 columns for a total of 114.688 pixels. The chip registers have been set with the same values used during the Test Beam at Desy (July 2022) which are different for the DC and AC-coupling case. They are called for simplicity "**GOE settings**" and they are reported in Table 1.1, where the different biasing voltages used to power up the chip are also added.

In Figure 1.7 are plotted all the s-curves of the all Normal flavor pixels. The width of the figure is a first indication of the threshold dispersion of the whole flavor.

The threshold and noise distributions measured on all pixels with the s-curve method, have been fitted with a gaussian distribution and they are shown in Figure 1.8 with their maps, too.

### 1.2.2.2 Cascode FE

**Cascode FE** is the second flavor and like the previous one, it consists of 512 rows and 224 columns for a number of total pixels equal to 114.688. For this flavor the same procedure of Normal FE has been followed and also the same registers' values (Table 1.1) have been used. In Figure 1.9 the s-curves of all pixels are shown.

Registers	Normal/Cascode FE ( $P_{SUB}/P_{WELL} = -3$ V)	HV/HV-Cascode FE ( $P_{SUB}/P_{WELL} = 0$ V, HV = +5 V)
$I_{THR}$	64	30
$I_{BIAS}$	50	60
$V_{RESET}$	143	100
$I_{CASN}$	0	8
$I_{DB}$	100	100
$I_{TUNE}$	53	53

Table 1.1: Settings of the main registers used for all flavors (W14R12 chip) during the Test Beam in Desy.

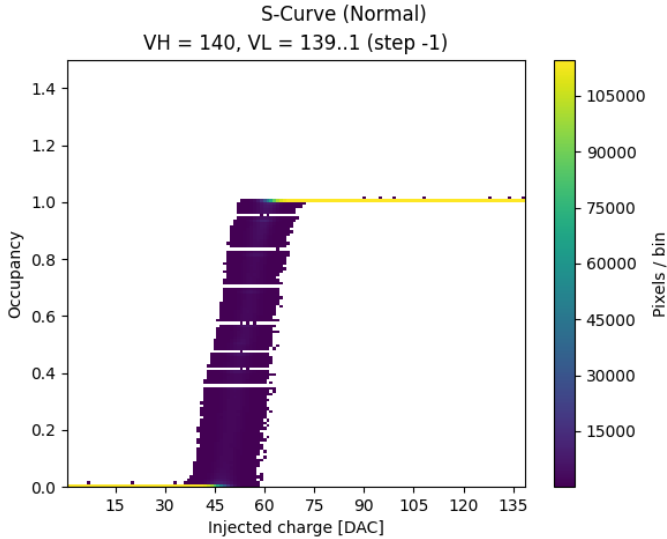


Figure 1.7: S-curves of all pixels of the Normal FE with a maximum injection pulse of 140 DAC.

The maps and the fit of the threshold and noise distributions instead, are shown in Figure 1.10.

### 1.2.2.3 HV-Cascode FE

The third flavor is **HV-Cascode FE** and it is composed by 512 rows and 32 columns for a total number of pixel equal to 16384. Also for these last two flavors, the main chip registers are set with the same values tested and used during the Test Beam (@Desy) (but different from those used for the first two flavors). They are reported in Table 1.1 .

As we can see from the plot of the alle s-curves in Figure 1.11, with this choice of registers there were a lot of "hot" pixels with occupancy > 1, but at this stage of measurements they were not masked. These hot pixels with occupancy > 1, register more hits than the number of injected events. This behaviour seems to indicate that they are stimulated, not by the charge injection, but by some other input, due to "cross-talk", active during the readout of the matrix. The origin of the hot pixel and cross-talk was carefully investigated later (see section 1.6) .

In Figure 1.12 are shown the fit of the threshold and noise distributions.

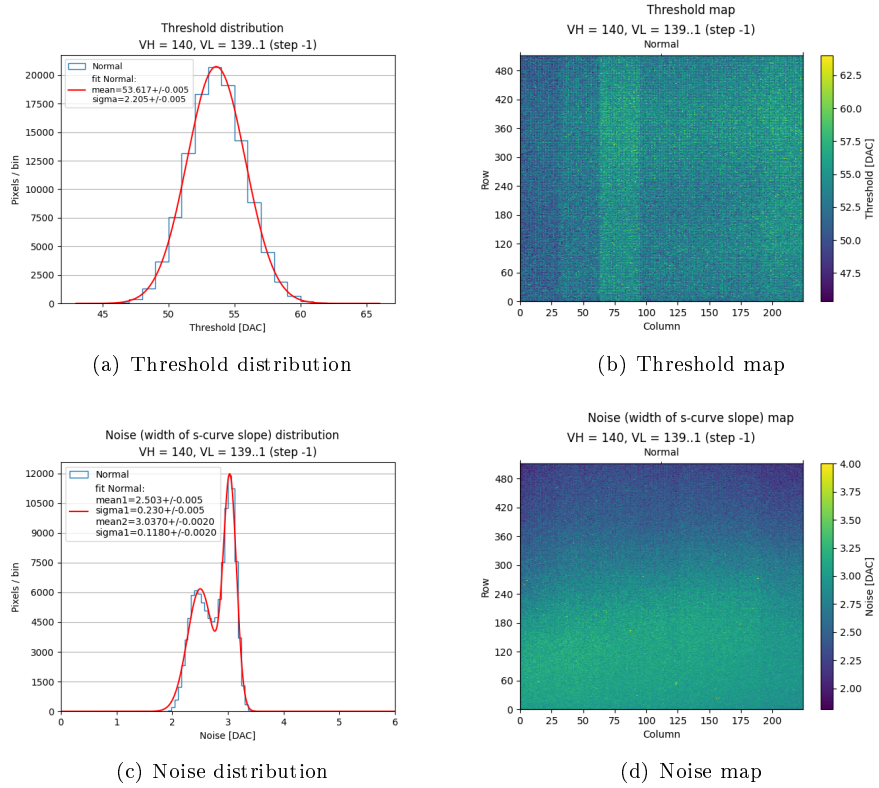


Figure 1.8: Normal FE.

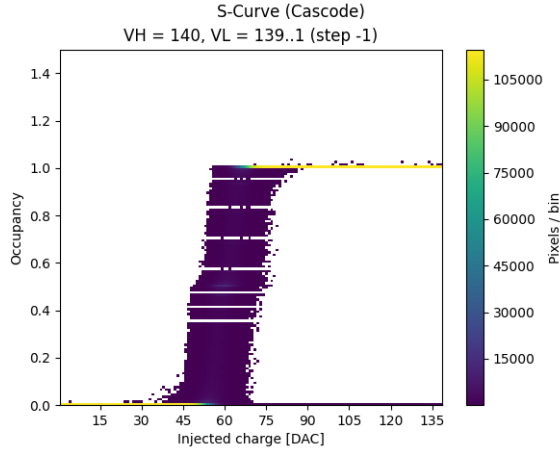


Figure 1.9: S-curves of all pixels in the **Cascode** flavor with a maximum injection pulse of 140 DAC.

#### 1.2.2.4 HV-Normal FE

The fourth and last flavor is the **HV-Normal FE** which has the same layout and so the same number of pixel of the previous FE. The main registers have been set with the values reported

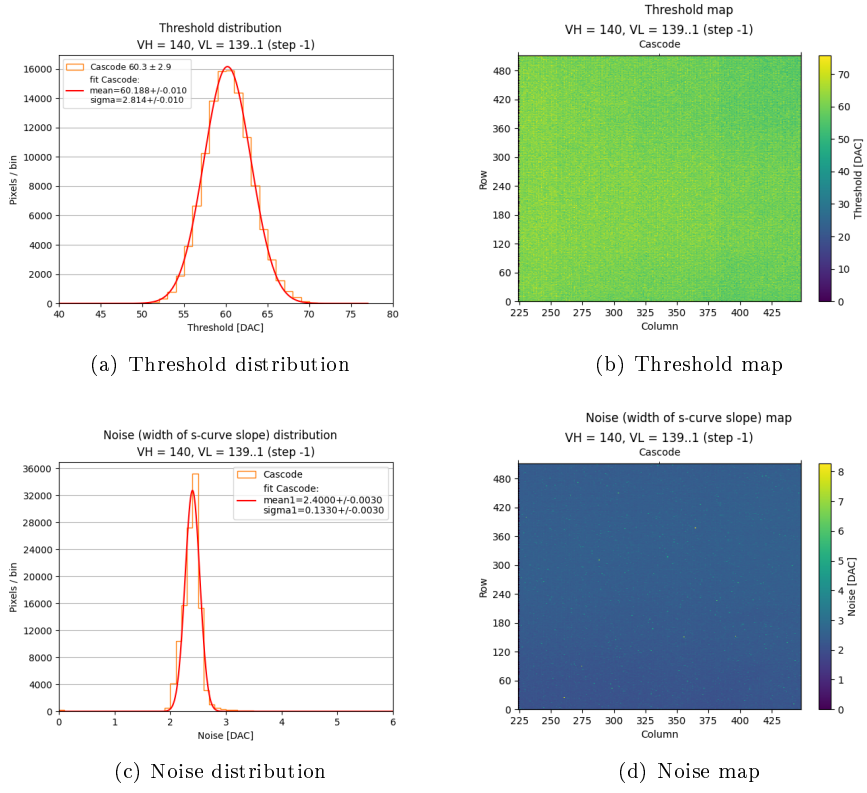


Figure 1.10: Cascode FE.

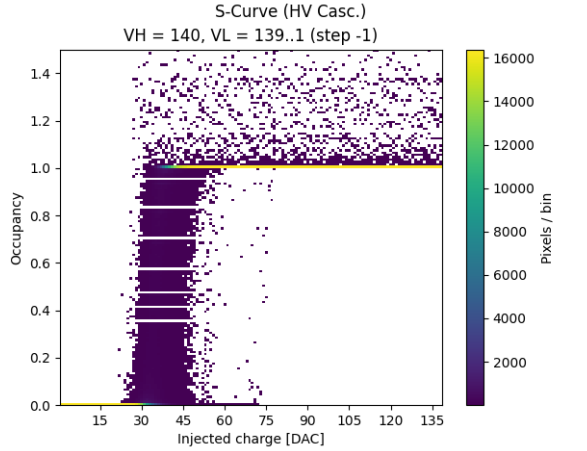


Figure 1.11: S-curves of all pixels in **HV Cascode** flavor with a maximum injection pulse of 140 DAC.

in Table 1.1. In Figure 1.13, the s-curves of all pixel in this flavor. Also here we can see that there were some hot pixels unmasked. Moreover the last 16 columns were not working (visible

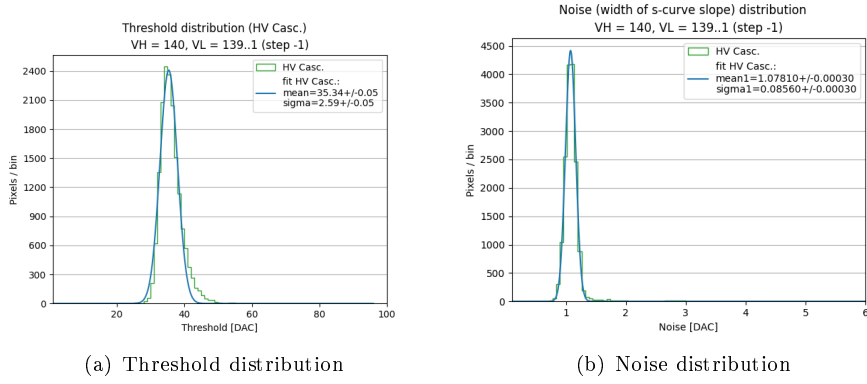


Figure 1.12: HV Cascode FE.

in the maps in Figure 1.15) and as a matter of fact they had return a peak of threshold near the value 0, which is excluded from the threshold distributions plots.

So actually in this part of the matrix, the real number of pixel studied was the half of the total, such as 8192 pixels.

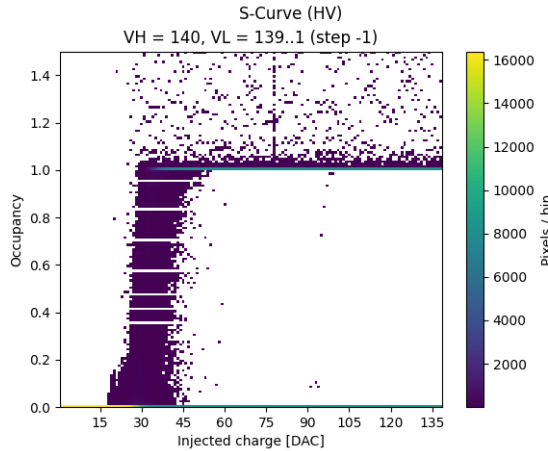


Figure 1.13: S-curves of all pixels in **HV Cascode FE** with an injection pulse of 140 DAC.

In Figure 1.14 the fit of the threshold and noise distributions.

At last, in Figure 1.15 the threshold and noise maps of the whole HV flavor.

As we will see in the following (section 1.6), the atypical s-curves in HVs flavors with many hot pixels, have been the first hint of the cross-talk problem, tied to a global lower threshold in these sectors, compared with the first two threshold measured in the Normal and Cascode sector (with the TB settings).

#### 1.2.2.5 Summary Table

In table on the following page a summary of results for threshold, noise and threshold dispersion of all FE.

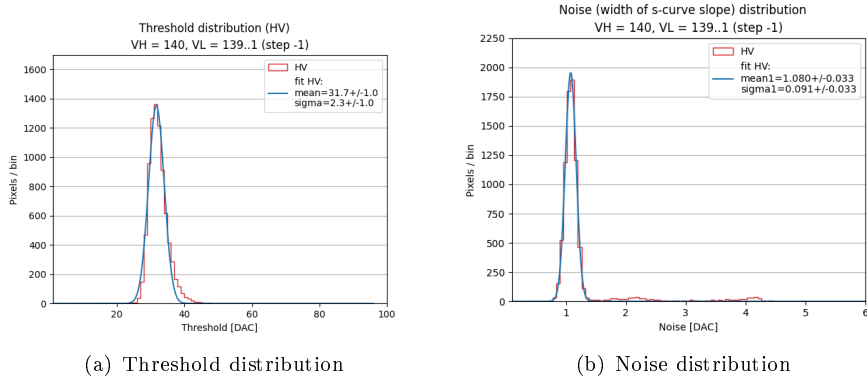


Figure 1.14: HV Normal FE.

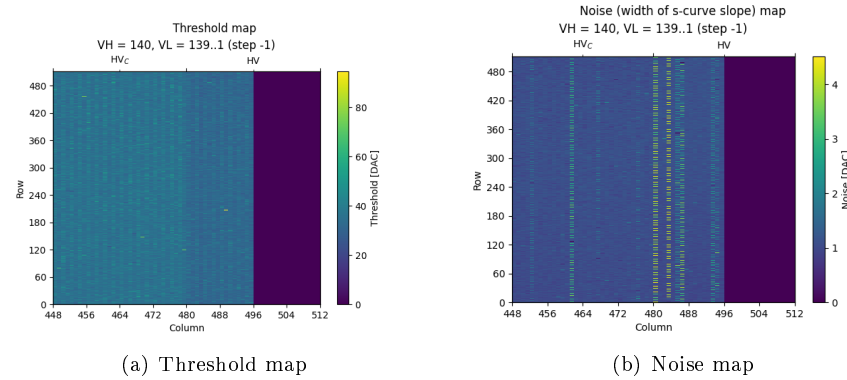


Figure 1.15: HV's FE.

Front-End	Threshold [ $e^-$ ]	Threshold dispersion [ $e^-$ ]	Noise [ $e^-$ ]
Normal	$53.62 \pm 0.01$	$2.21 \pm 0.01$	$2.503 \pm 0.005$
Cascode	$60.19 \pm 0.01$	$2.81 \pm 0.01$	$3.037 \pm 0.002$
HV - Cascode	$35.34 \pm 0.05$	$2.59 \pm 0.05$	$1.0781 \pm 0.0003$
HV	$31.70 \pm 0.10$	$2.30 \pm 0.10$	$1.080 \pm 0.033$

Table 1.2: Summary table of threshold and noise values for all flavors of the W14R12 chip.

### 1.2.3 Threshold dispersion and tuning

TJ-Monopix 2 is equipped with a circuit which allows the *threshold tuning*. We have already mentioned that the analog part of the in-pixel front-end (Figure 1.4) includes the 3-bit threshold tuning DAC, that can be used to adjust the discriminator threshold of each pixel with respect to the global chip threshold level thus reducing the threshold dispersion. In other words it can adjust every pixel threshold, in order to have a threshold on the matrix as uniform as possible, or in any case a dispersion as small as possible, which is especially important to operate the matrix with low threshold, needed with the reduced collection efficiency due to radiation damage. This system has been designed in order to counteract some negative effects that affect the threshold

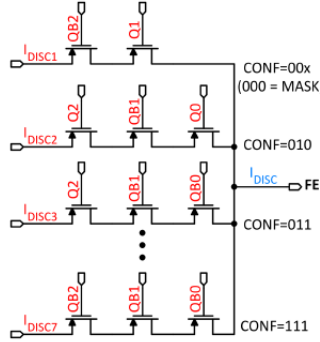


Figure 1.16: Schematic of 3-bit tuning DAC (TDAC)

dispersion like systematics (for example related to biasing), process and temperature variations and radiation damage.

Specifically the TDAC circuit, shown in Figure 1.16, helps to make threshold trimming of each pixel. This component controls the discriminator active load current  $I_{DISC}$  which is partially responsible of the pixel threshold. It works as an analog multiplexer (consisting of simple PMOS transistor switches), which selects one of seven  $I_{DISC,n}$  lines generated by the main 8-bit biasing DAC. So the possible value of the final  $I_{DISC}$  is given by the sum of two contributions:

$$I_{DISC} = I_{DISC,coarse} + (TCODE - 1) \cdot I_{DISC,fine}, \quad \text{where} \quad 1 \leq TDAC \leq 7 \quad (1.3)$$

$I_{DISC,coarse}$  is the current set by the primary value of threshold, resulting by the setting of the main registers which are responsible for it (listed in ...).  $I_{DISC,fine}$  is the current selected by the fine tuning step (TDAC) and it depends on the 3-bit tuning code that is stored in the in-pixel tuning memory latch (the in-pixel configuration memory). **TCODE** is the decimal representation of the TDAC code.

For example if the 3-bit DAC are set to "111", the decimal representation is 8 and the fine tuning provide a current  $I_{DISC,7}$ , which corresponds to the highest threshold. If the 3-bit are set to "010" the corresponding TCODE is 2 and the current  $I_{DISC,1}$  is provided, which set the lowest threshold possible around the central value  $I_{DISC,coarse}$ . The particular combination "000" instead (TCODE = 0) masks the pixel by disabling the discriminator, without affecting the operation of the others.

### 1.2.3.1 First results from threshold tuning

It has been trying to apply the fine tuning method to level out the threshold of some pixels as much as possible. We have considered about 12.000 pixels of the **Cascode FE** and in Figure 1.17 are shown the results before and after the threshold trimming for the s-curves and threshold distributions.

As we can see the dispersion has been reduced of the 42% after the tuning and as consequence also the estimation of the threshold is more precise. In figure on page 18 are displayed the maps of the threshold and of the TDAC values, such as the value of TCODE assigned at each pixel, in order to obtain a threshold as uniform as possible.

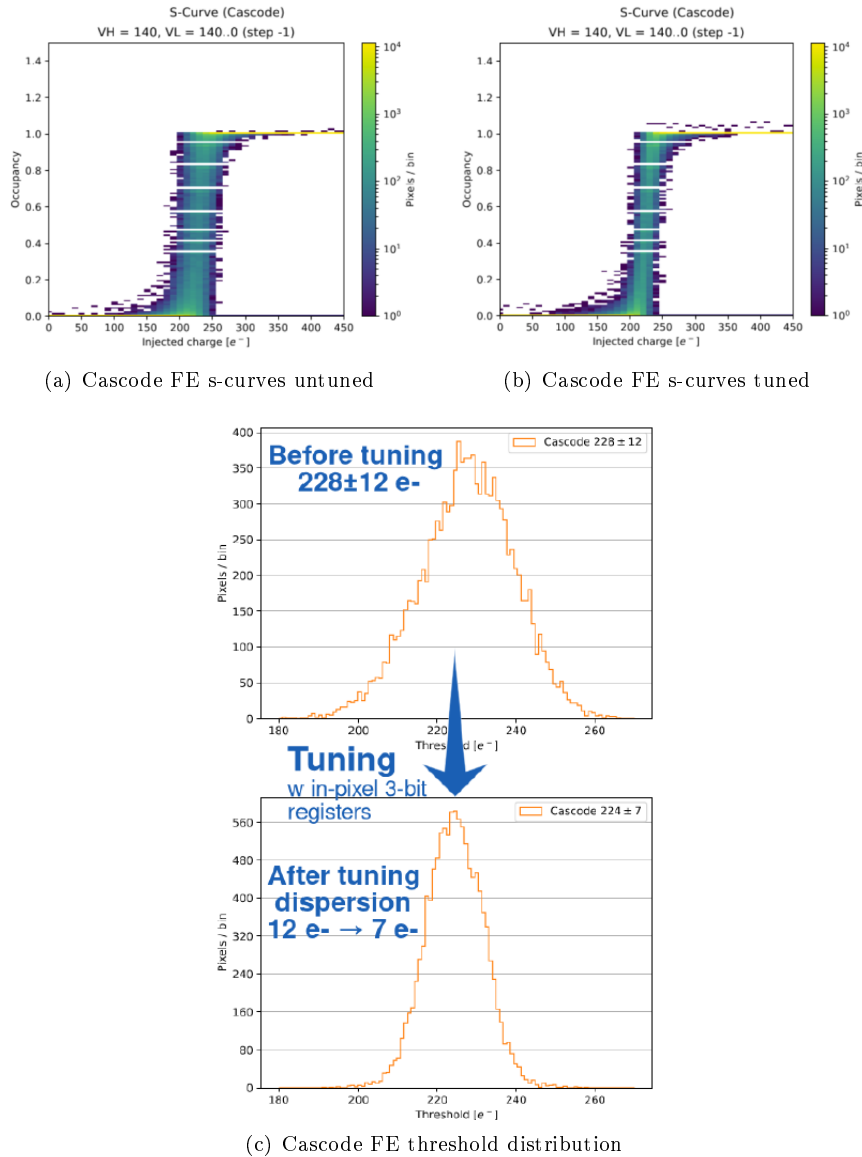


Figure 1.17: Cascode FE before tuning and after tuning comparison.

### 1.3 ToT calibration with internal injection

The analog information on the signal height is provided by the Time Over Threshold (Figure 1.19) digitized with a 25 ns clock (the BCID clock).

As it has been pointed out in the previous, the choice to use a simple diode instead of a PMOS transistor as reset input baseline element, increases the tolerance to TID radiation but at the same time it implicates a non-linear relationship between the injected charge and the ToT. For this reason, one of the goal of this analysis was to measure the calibration curve ToT vs

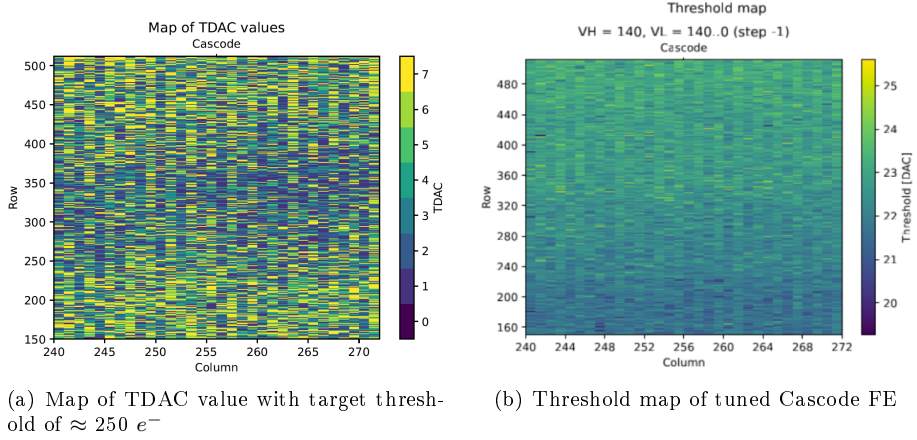


Figure 1.18: Maps of tuned Cascode FE.

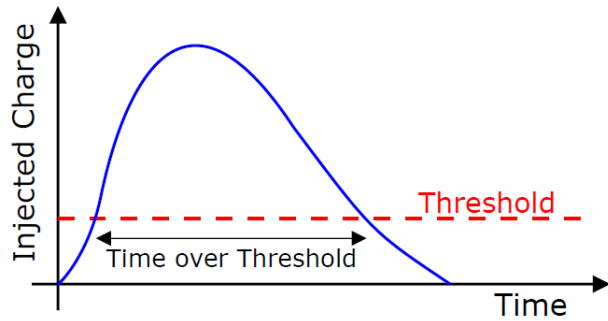


Figure 1.19: ...

$Q_{inj}$  via the internal injection. The fit to the calibration curve allows to find the conversion factor needed to reconstruct the signal amplitude. It also allows an absolute calibration of the injection capacitance comparing the results with the ToT response from the radioactive source with known released signal.

In carrying out the measurements mentioned above, we started to notice some issues with the injection circuit, which showed some saturation in the voltage pulse at high values of the registers. Due to this issue, the ToT response to internal injection could only be measured up to 170 DAC ( $\approx 1700 e^-$ ). This was enough for the absolute calibration using the  $^{55}\text{Fe}$  5.9 KeV line ( $\approx 1616 e^-$ ) as explained below.

A method has been therefore devised to obtain reliable values of threshold and ToT up to a value of 170 DAC of effective charge injected.

The calibration function adopted to describe the  $Q_{inj}$ -ToT relationship was then used to extrapolate ToT values in the region of high charge (above 170 DAC,  $\approx 1700 e^-$ ) not accessible with the injection circuit, to compare with the emission peaks of other radioactive sources and explore a larger range.

### 1.3.1 Time Over Threshold (TOT) curves and fit

The ToT vs  $Q_{inj}$  responses for the four flavors of the matrix (using the same TB register settings) are shown in Figure 1.20. The function chosen to describe the calibration curves is:

$$y(x) = a \cdot x + b - \frac{c}{x - t} \quad (1.4)$$

with  $a$ ,  $b$ ,  $c$  and  $t$  free parameters and where the  $y$  represents the ToT corresponding to a precise value of collected charge, express by  $x$ .

Actually we know that the ToT distribution starts to grow near the threshold, so one of the four free parameters could be computed in function of the threshold value estimated from the previous measurements reported in section 1.2.2.

In more details, knowing that  $y(x_{th})$  must be equal to 0 that is the ToT value at the threshold, it can be imposed for example:

$$0 = a \cdot x_{th} + b - \frac{c}{x_{th} - t} \Rightarrow c = x_{th}^2 \cdot a + x_{th} \cdot (b - a \cdot t) - t \cdot b \quad (1.5)$$

In this way the number of parameters to fit is reduced. In principle a similar equation could be equivalently solved for  $a$ ,  $b$  and  $t$ .

Thus different fits have been made: one imposing a constraint on a free parameter (like shown above) and the other one leaving all parameters free. For all of them the value of  $\chi^2$  (MSE) have been computed and for all flavors it had its minimum when no parameters were fixed. So in the following the results from these last fits with all the parameters left free, have been considered.

The same data collected in the previous measurements of thresholds have been used to fit the ToT curves of all pixels for each frontend. As a matter of fact we want to fully characterized the chip response with "GOE" settings (Table 1.1), in order to use the results to convert ToT to charge collected for the analysis of the TB data. In Table 1.3 are reported the results of the fits for all parameters.

	<b>Normal</b>	<b>Cascode</b>	<b>HV Cascode</b>	<b>HV</b>
$a \pm \Delta a$ [ $\frac{\text{ToT}}{\text{DAC}}$ ]	$0.12 \pm 0.07$	$0.12 \pm 0.01$	$0.257 \pm 0.007$	$0.275 \pm 0.008$
$b \pm \Delta b$ [ $\text{ToT}$ ]	$4 \pm 18$	$1.4 \pm 3.1$	$3.2 \pm 1.4$	$2.3 \pm 1.6$
$c \pm \Delta c$ [ $\text{ToT} \cdot \text{DAC}$ ]	$200 \pm 1100$	$140 \pm 130$	$160 \pm 70$	$140 \pm 80$
$t \pm \Delta t$ [ $\text{DAC}$ ]	$20 \pm 90$	$40 \pm 15$	$17 \pm 6$	$13 \pm 8$

Table 1.3: Parameters obtained from the fit of ToT curve for each frontend.

## 1.4 Response to radioactive source and absolute calibration

The absolute calibration of the matrix consists in characterizing the response of each pixel to a known signal, like the emission peaks of radioactive sources, then comparing the results with the response from the internal injection circuit to the same amount of charge. By the means of the  $Q_{inj}$  - ToT fit (section 1.3.1), it is possible to convert the ToT signal value to collected charge. Three different X-rays radioactive sources were used to study the signal spectrum of the matrix, with emission lines from 6 to 60 KeV (corresponding approximately to 1600 and 16000 e- respectively). In fact the knowledge of the sources emission spectrum (in other words, the charge released in the matrix from particles emitted in decays) allows to compare the spectra obtained irradiating the chip, with the expected value of their peaks. It is worth mentioning that only

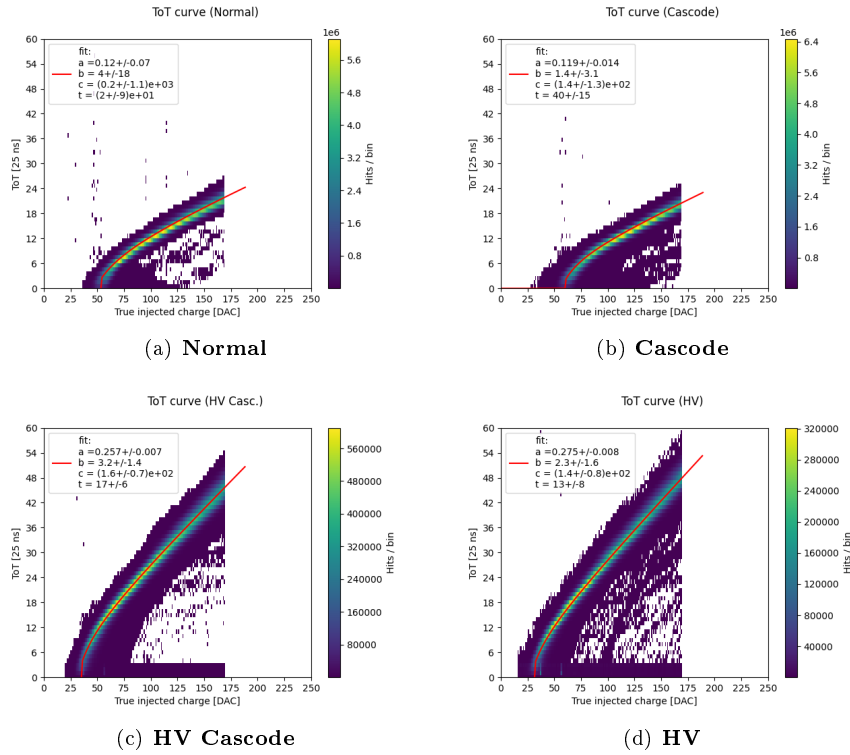


Figure 1.20: ToT curves fit for all frontend.

the events in which all charge induced is collected in a single pixel are part of the peaks reconstructed by the chip.

The absolute calibration of the conversion factor of equation 1.1 (i.e. of the injection capacitance  $C_{inj}$ ) is performed with the 5.9 KeV peak of the  $^{55}\text{Fe}$  source (*approx* 1616  $e^-$ ), that is still in the range explored with the injection circuit. The other radioactive sources allowed to extend the ToT comparison(?) at higher values with respect to the limit imposed by the saturation of the internal injection circuit. In Table 1.4 are shown the energies of the  $\gamma$  emitted by the sources used.

Considering that the average energy necessary to produce an electron/hole pair in silicon is 3.65 eV, it is possible to convert the peak energies in a mean value of electrons released using the equation 1.6. So in Table 1.4 are reported also the equivalent emission in electrons, which will be useful later.

$$N_{e^-} = \frac{E [eV]}{3.65 \left[ \frac{eV}{e/h \text{ pair}} \right]} \quad (1.6)$$

Now we can go through the results obtained from three different sources:  $^{55}\text{Fe}$ ,  $^{241}\text{Am}$  and  $^{109}\text{Cd}$ .

Source	Energy $\gamma$ [KeV]	Equivalent charge [ $e^-$ ]
$^{55}\text{Fe}$	5.9	1616
$^{241}\text{Am}$	13.9	3808
$^{241}\text{Am}$	17.7	4849
$^{241}\text{Am}$	20.7	5671
$^{109}\text{Cd}$	22	6027
$^{241}\text{Am}$	26.4	7233
$^{241}\text{Am}$	59.7	16356

Table 1.4: Emission lines of  $^{55}\text{Fe}$ ,  $^{241}\text{Am}$ ,  $^{109}\text{Cd}$  sources visible by the sensor.

#### 1.4.1 $^{55}\text{Fe}$

The  $^{55}\text{Fe}$  source decays by **electron capture** to  $^{55}\text{Mn}$ . One of the photons emitted in this transition has an energy of 5.9 KeV ( $K_\alpha$ ) and it produces via photoelectric effect an electron, which deposits a ionization charge of about 1616  $e^-$  in the sensor. All flavors were exposed to a  $^{55}\text{Fe}$  source, with activity of 18 MBq. In Figure 1.21 are shown the results for the ToT spectrum of single pixels. The peak corresponds to events where the  $\gamma$  interacts close to the collection diode and the entire signal is on a single pixel. The shoulder at smaller ToT is due to the charge sharing among several pixels, since no clusters are reconstructed. The peak was fitted by a gaussian function, limited in the region of the peak itself.

As it can be seen for the HV's FE a cut has been applied at low ToT, only to make clearly visible the emission line, since a lot of noisy pixels caused a sharp peak at 0 ToT. In those flavors there were several columns of not-functioning pixels. In the box of each plot are also reported the results of the fit that will be crucial in the following.

#### 1.4.2 $^{241}\text{Am}$

The  $^{241}\text{Am}$  source has a more complex spectrum (Figure 1.22) and not all its peaks can be detected by the chip (because of the limited range of ToT available, depending on the number of bits dedicated to it). The spectrum shows other minor peaks besides the usual intense gamma peaks (59.5 and 26.3 keV) and several characteristic L X-rays from  $^{237}\text{Np}$  (20.7, 17.7 and 13.9 keV).

The ToT measured spectra with the  $^{241}\text{Am}$  source on the four flavors are reported in Figure 1.23. Two peaks at lower energy are clearly visible while, for higher ToT values there are larger structures.

In the case of the first two flavors, it could be possible to fit four peaks of the emission lines. In case of the HV's flavors instead, only three peaks for the HV-Cascode FE and two for the HV. As already discussed (section on page 7) the AC-coupling causes about 41.5% of signal loss, so they are much less evident and more difficult to fit as isolated peak.

#### 1.4.3 $^{109}\text{Cd}$

The third source employed was the  $^{109}\text{Cd}$ . This isotope decays in  $^{109}\text{Ag}$  by electronic capture, producing a photon of 22 KeV in the transition. The ToT measured spectra with  $^{109}\text{Cd}$  source on the four flavors of the matrix are reported in Figure 1.24.

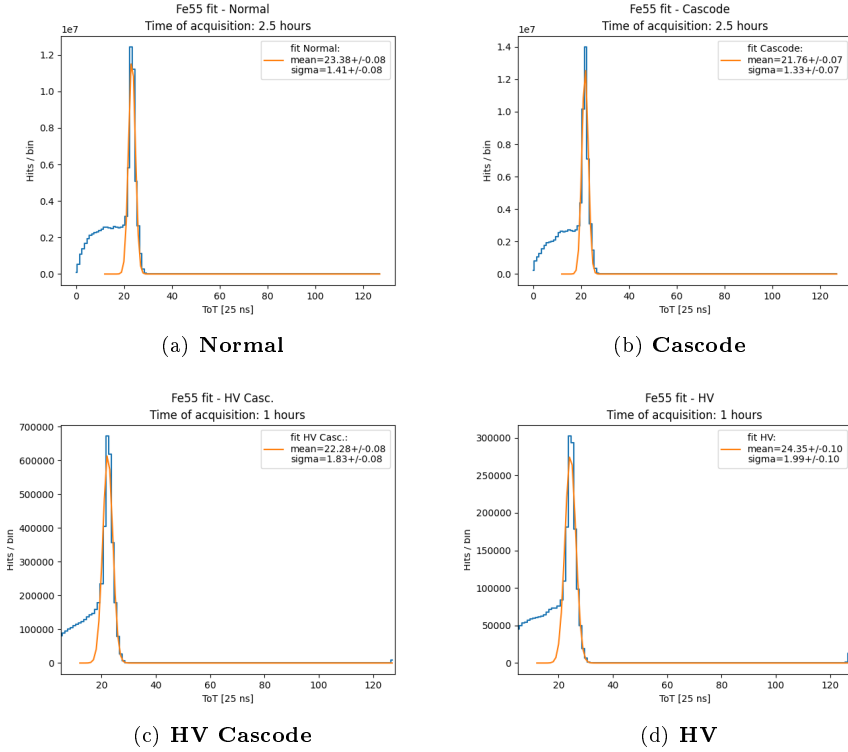


Figure 1.21:  $^{55}\text{Fe}$  peaks for all frontends.

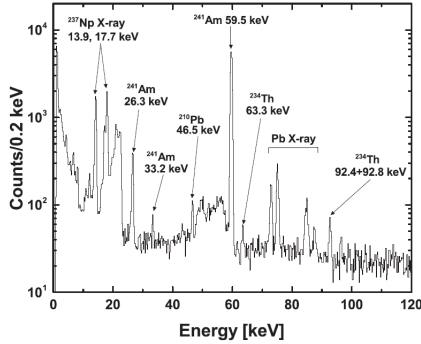


Figure 5. Gamma-ray spectrum of the  $^{241}\text{Am}$  source.

Figure 1.22:  $^{241}\text{Am}$   $\gamma$  emission spectrum.

#### 1.4.4 Injection capacitance calibration

The absolute calibration of the injection capacitance and of the conversion factor  $K$  of equation 1.1, that convert a signal charge expressed in DAC units to  $e^-$ , is performed using the data from the  $^{55}\text{Fe}$  source.

As first step the ToT of the peak of the 5.9 KeV  $\gamma$  line is converted to signal charge in DAC

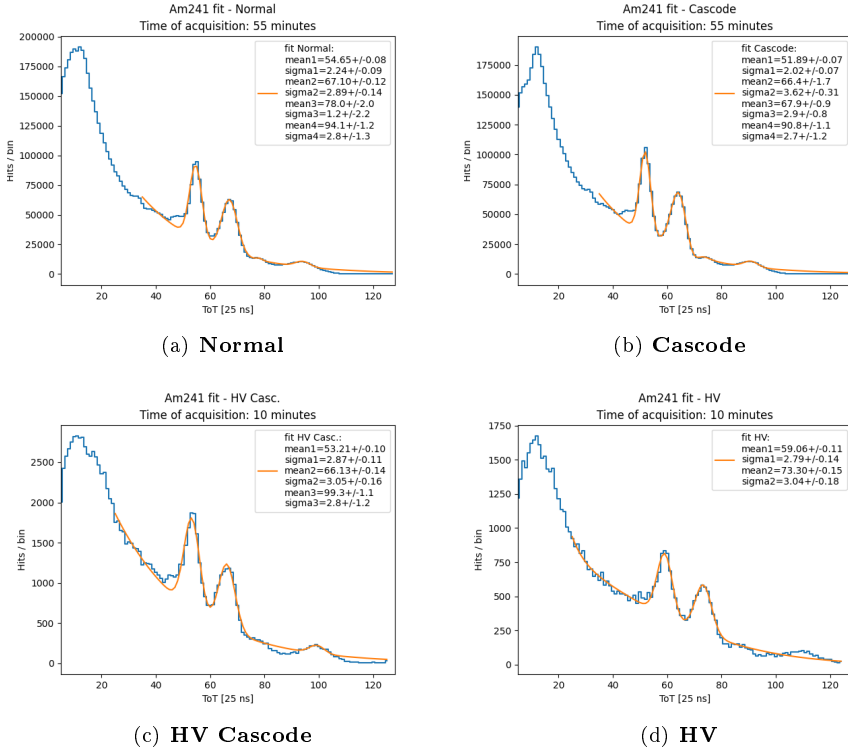


Figure 1.23:  $^{241}\text{Am}$  peaks for all frontends.

using the fitted calibration curve of equation 1.4

Specifically the fit function was inverted obtaining:

$$x(y) = \left( \frac{t}{2} - \frac{b}{2a} + \frac{y}{2a} \right) \pm \sqrt{\left( \frac{t}{2} + \frac{b}{2a} - \frac{y}{2a} \right)^2 + \frac{c}{a}} \quad (1.7)$$

where  $x$  represents the charge in DAC corresponding to the ToT labeled by  $y$ .

As shown in Table 1.4, the charge released in the sensor by the 5.9 KeV  $\gamma$  corresponds roughly to  $Q_{5.9\text{ KeV}}(e^-) = 1616 e^-$ . Therefore the conversion factor  $K$  for each pixel can be calculated as:

$$K \left[ \frac{e^-}{DAC} \right] = \frac{1616 e^-}{Q_{5.9\text{ KeV}}[DAC]} \quad (1.8)$$

By these steps, a value of the conversion factor was estimated for each well-functioning pixel. In Figure 1.25 is reported the distributions of the conversion factor estimated, fitted by a gaussian function.

????????????? Here it is necessary to point out that for iron source more statistics were collected so in this case a complete analysis of each pixel has been done. For the other sources instead, there weren't enough statistics on every pixel so the injection capacitance has been estimate only as a mean value for the whole front-end, just to compare with the results obtained from the iron analysis. In case of  $^{55}\text{Fe}$  source, we managed to fit the emission peak for each

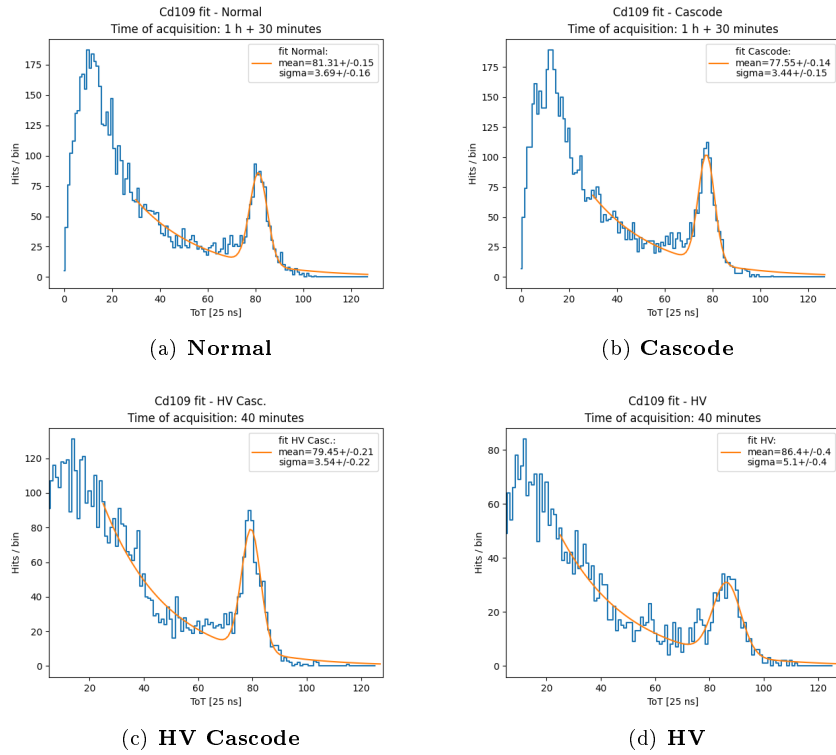


Figure 1.24:  $^{109}\text{Cd}$  pekas for all frontends.

Source peak	$K_{Normal}$	$K_{Cascode}$
$^{55}\text{Fe}$ (5.9 KeV)	9.37	9.00
$^{241}\text{Am}$ (13.9 KeV)	8.94	8.91
$^{241}\text{Am}$ (17.7 KeV)	9.16	8.84
$^{241}\text{Am}$ (20.7 KeV)	9.15	10.11
$^{109}\text{Cd}$ (22 KeV)	9.32	9.39
$^{241}\text{Am}$ (26.4 KeV)	9.60	9.61
Mean value	9.26	9.31

Table 1.5: Estimation of injection capacitance of Normal and Cascode flavors for different source emission peaks.

working pixel of the whole matrix.

???????????????

#### 1.4.5 Check on calibration curve ToT vs $Q_{inj}$ with radioactive sources

The calibration of the ToT vs  $Q_{inj}$ (DAC) with the injection circuit could be performed only up to  $\approx 170$  DAC. Th radioactive sources can be used up to higher energy to check the agreement

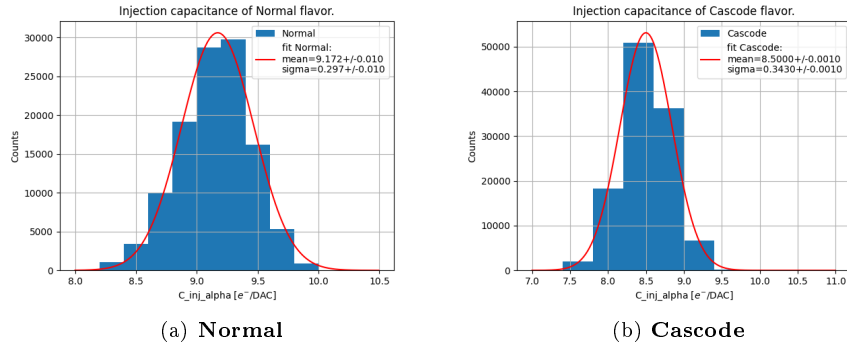


Figure 1.25: Injection capacitance distributions of Normal and Cascode FE.

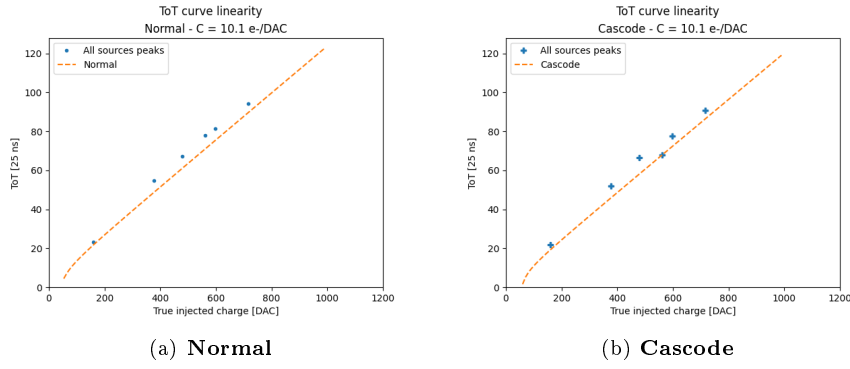


Figure 1.26: ToT of all flavors assuming the nominal(expected) conversion factor equal to 10.1  $\frac{e^-}{DAC}$ .

with the fitted function in equation 1.4 .

Initially the signal charge in DAC corresponding to each  $\gamma$  peak, has been calculated using the nominal conversion factor equal to  $10.1 \frac{e^-}{DAC}$ . As it could be seen from results in Figure 1.26 there isn't good agreement between data and ToT relationship studied in section 1.3.1.

After the absolute calibration, assuming the average value of the conversion factor  $K$  (*Mean value*) measured with  $^{55}\text{Fe}$ , the charge in DAC corresponding to the emission peaks have been recalculated and results are shown in Figure 1.27.

As we can see, a better agreement is therefore obtained and this shows that through calibration we are now able to interpret data with greater precision, which was the main purpose of this analysis.

## 1.5 Operation with low threshold

One of the most important target in sensor design is to keep high efficiency even after irradiation damages. All experimental environments indeed, are exposed to high doses of radiations, so it's crucial to ensure the functionality of the detectors, even after being irradiated.

For this reason, many tests were done in order to understand the chip behaviour at low

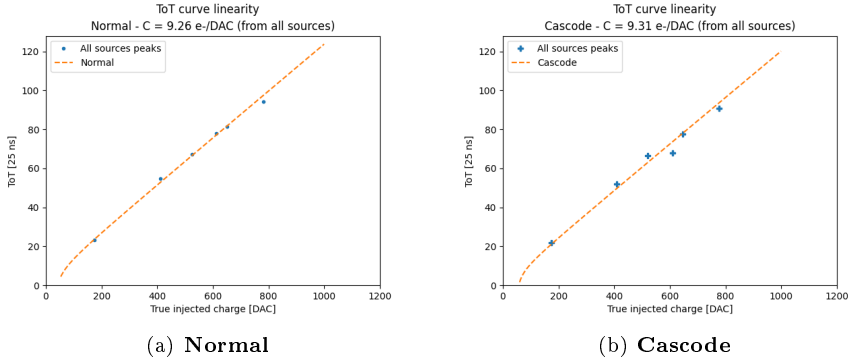


Figure 1.27: ToT linearity of all flavors assuming the conversion factor obtained from calibration for each FE.

threshold where a good value of efficiency could be preserved. Moreover working at low threshold allows to detect low charge events due to charge sharing or charge trapping (effect which increases after irradiation), especially in case of thin epitaxial material.

### 1.5.1 Register optimization

As we have seen in section (REFERENCE), there are a lot of registers which control the discriminator threshold and also the readout sequence. So preliminary it was necessary to explore their possible settings in order to operate the chip at low threshold.

Now we will go through the main registers used for this purpose, in order to explain their functionality. There are several dozens of registers but we focused on some of the most important and crucial to set the threshold and its dispersion.

- $I_{CASN}$ : this current is responsible of the output baseline signal. In particular it sets the baseline of the FE output that goes to the input discriminator. In a few words, higher this value, higher the baseline, lower the threshold and also a little bit the gain and vice versa by decreasing it.
- $I_{THR}$ : it controls the pre-amplifier feedback strength and speed, so it is responsible for the output reset rate. Increasing this current increases the gain and the time that the analog output takes to get back to the baseline and as consequence, it increases a lot the maximum value of the ToT. In fact it is recommended to set  $I_{THR}$  to low value (e.g. 8 nA[ref]) in order to avoid high ToT slope.
- $I_{DB}$ : this current corresponds to  $I_{DISC,coarse}$  explained in section ?? on page ???. It represents the primary current that sets the discriminator threshold, to which another current is added by the tuning.
- $I_{TUNE}$ : it corresponds to  $I_{DISC,fine}$  instead (always section on page ??). Remembering the equation from tuning <sup>1</sup> (on page ??), this is the current to multiply by the TDAC value, which is added to  $I_{DB}$ , during the tuning process.

---

<sup>1</sup>

$$I_{DISC} = I_{DISC,coarse} + (TCODE - 1) \cdot I_{DISC,fine}, \quad \text{where} \quad 1 \leq TDAC \leq 7 \quad (1.9)$$

- $I_{BIAS}$ : this current acts on the pre-amplifier input transistor and influences the threshold dispersion and the gain. In particular increasing this value, the dispersion decreases and the gain becomes greater. Nevertheless it can't be increased a lot because it affects the power consumption, too.
- $V_{RESET}$ : this register influences the threshold dispersion. Lowering its value, the dispersion decreases and vice versa.

### 1.5.2 Comparison between data and simulation

In the interest of understanding how the registers' setting of the chip influences the threshold, several measurements have been taken with different configuration of their values. The results are compared with simulations done by Hung Pham. (...). [???

$I_{CASN}$

In figure 1.28, we can see the simulated behaviour of the threshold and the gain, increasing the value o  $I_{CASN}$ .

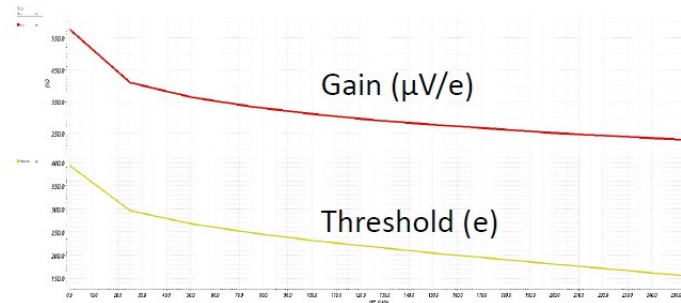


Figure 1.28: Trends of Gain and Threshold increasing  $I_{CASN}$ .

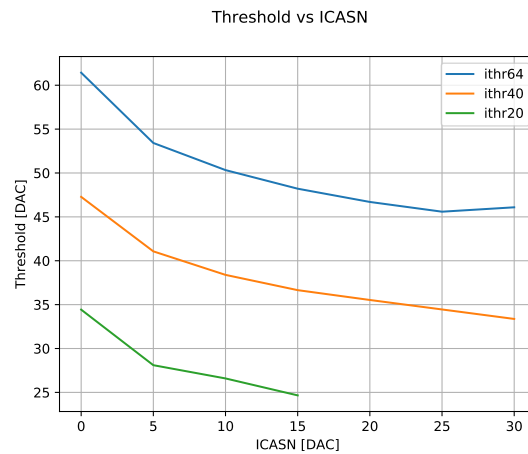


Figure 1.29: Threshold vs.  $I_{CASN}$  for  $I_{THR}= 20, 40, 64$ .

To verify the trend of threshold as this current varies, three different acquisitions have been taken by fixing  $I_{THR} = 20, 40, 64$  and increasing  $I_{CASN}$  from 0 to 30 DAC, with a step of 5 DAC. We have done this enabling 200 pixels in the Cascode FE (rows: 472 - 512, cols: 225 - 230).[??]

Each threshold distribution has been fitted with a gaussian function in order to estimate the average threshold value and its dispersion.

In figure 1.29 on the previous page are reported all trends obtained.

$I_{THR}$

Reusing the same data of the previous measurements, the trend of the threshold have been studied by changing the value of  $I_{THR}$  and fixing that of  $I_{CASN}$ . In this case only  $I_{CASN}$  from 0 to 15 DAC is considered, because for higher values we don't have enough measures of the threshold (specifically only two for  $I_{THR}=40, 64$ ). The results are shown in figure 1.30.

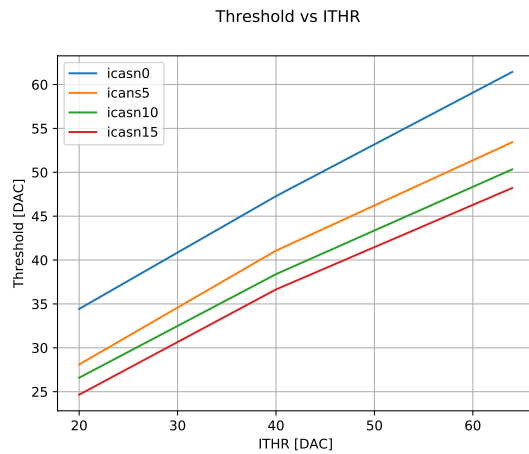


Figure 1.30: Threshold vs.  $I_{THR}$  for  $I_{CASN} = 0, 5, 10, 15$ .

As expected, increasing  $I_{THR}$  results to lower gain and faster return to baseline, so higher threshold. We can compare them with the simulation shown in figure 1.31 on the next page.

### Time over Threshold (ToT)

The last analysis done to make a comparison with the simulations, is about the trend of the ToT changing the value of  $I_{CASN}$  for a fixed value of  $I_{THR}$  and vice versa. In particular we consider the data obtained with  $I_{CASN}$  fixed to 0 DAC and  $I_{THR}$  to 64 DAC, which are the values studied and used for these registers during the Test Beam in Desy.

Results are reported in figure on page 30 and on page 31. Also here we can see a good agreement between data and simulations.

#### 1.5.2.1 some nice picture of the optimized thr and tuning

!!!!

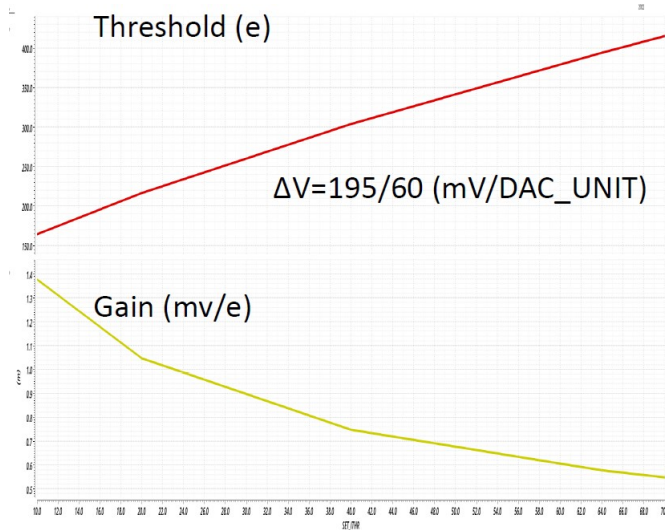


Figure 1.31: Trends of Gain and Threshold increasing  $I_{CASN}$ .

## 1.6 Cross talk issue and mitigation

As it was already pointed out, during the measurements of the average threshold of all FEs, there were something atypical in the s-curves of the HV flavors (subsection ?? on page ??), indeed some pixels seem to have occupancy greater than 1. This behavior threatens the good functionality of the overall matrix response, because these *noisy pixels* flood the readout, giving unreliable results.

Also the systematic study of different register configurations has revealed the presence of the hot pixels which prevent to use certain settings and as consequence to reach lower global thresholds.

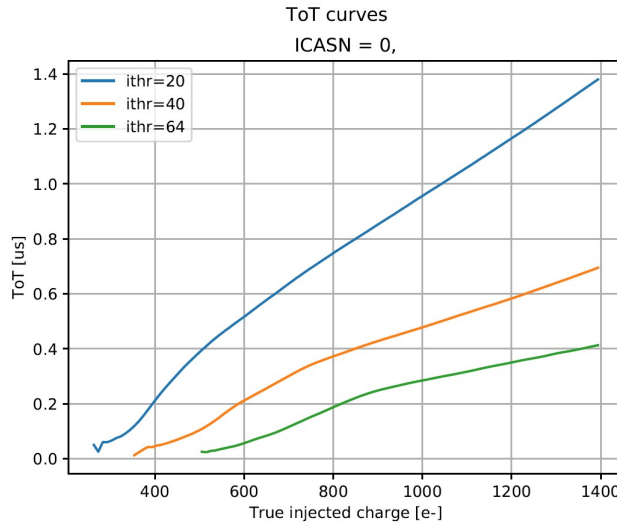
For this reason an investigation has been conducted in order to understand the reasons why they start to fire and how to cure them as far as possible. In the meantime an important issue with cross-talk of the readout signals was discovered, and so in this section we examine this effect and some attempts to mitigate it using different settings/bias.

### 1.6.1 Hot pixel issue

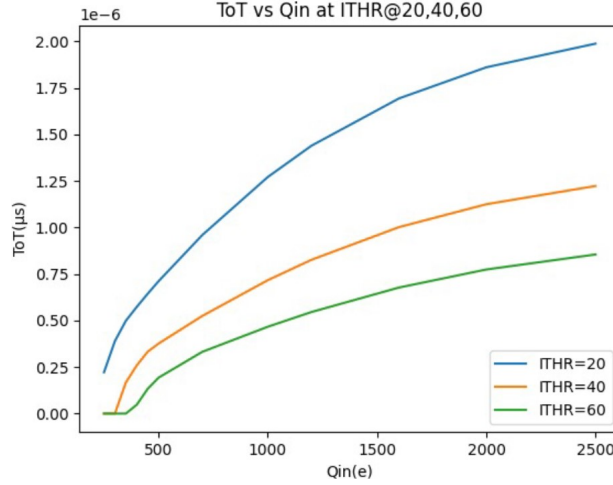
First of all we noticed that in the s-curves oh the HV flavors (e.g. that of HV-Cascode reported in figure on page 32), the atypical behavior could be triggered by a digital signal sent to the matrix during the readout activity at low threshold. This consideration is based on two main reasons:

- when the matrix has high threshold, like for Normal and Cascode FE, all pixels seem to behave as expected, without *hot pixels*.

Lowering the threshold and running some source acquisitions without any source, no strange behaviour was observed. Acquiring data with a radioactive source instead, even Normal and Cascode FE seem to reveal the same problem. This led to thinking that during the readout of good pixels an induced signal is created which couples with some other pixels,



(a) ToT vs  $I_{THR}$  ( $I_{CASN}=0$  DAC) - Data (Cascode)

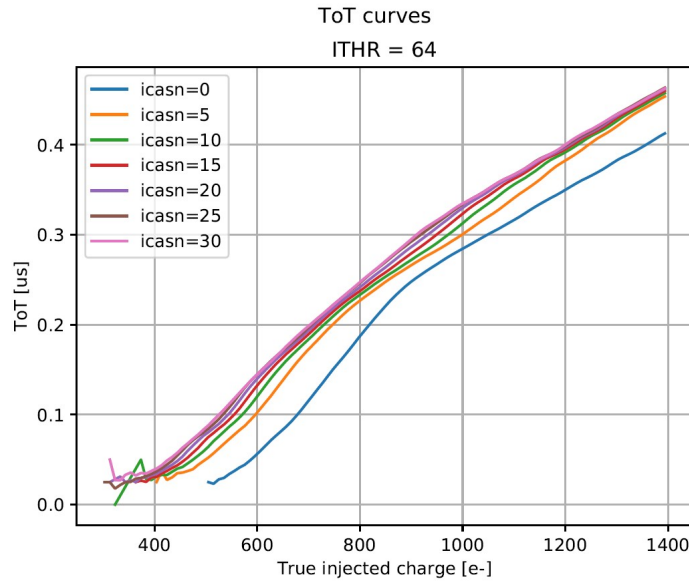


(b) ToT vs  $I_{THR}$  ( $I_{CASN}=0$  DAC) - Simulation

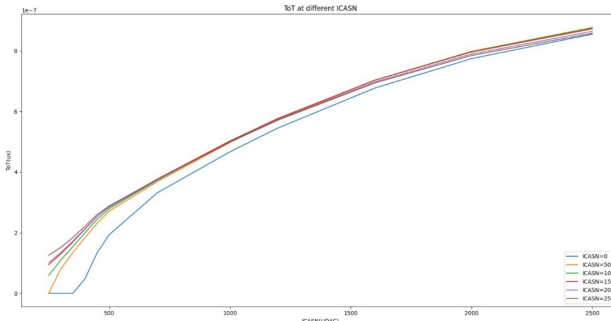
Figure 1.32: ToT vs  $I_{THR}$

in particular with those at lower threshold with respect to the average value. If the height of this signal exceeds the threshold of the single pixel, it causes some spurious hits, making the pixel "**hot**".

- Moreover, always considering the HV Cascode s-curves, it could be noticed that in the region before the threshold ( $Q_{inj} < \text{threshold}$ , pointed by the blue arrow) there isn't an anomalous activity which means that the induced signal is not due to the BCID tha is always sent to the matrix during the injection or an acquisition with the source, regardless of being above or below the threshold. The atypical behaviour indeed, is in the region above the threshold ( $Q_{inj} > \text{threshold}$ , pointed by the red arrow) where the occupancy of some pixels becomes greater than 1. This means that these *hot pixels* detect more hits of



(a) ToT vs  $I_{CASN}$  ( $I_{THR}=64$  DAC) - Data (Cascode)



(b) ToT vs  $I_{CASN}$  ( $I_{THR}=64$  DAC) - Simulation

Figure 1.33: ToT vs  $I_{CASN}$

those injected.

From these first observations, we have reached the conclusion that the cross talk could be tied to the readout activity. So we have started investigating the timestamp of those hits not synchronize with the timestamp of the injection.

### 1.6.2 Hot pixel strategy (study)

At first, it has been lowered the threshold in order to "create" hot pixel also in the first two flavors of the matrix. In fact with TB settings the threshold was too high and the hypothetical induced signal did not cause spurious hits. For this purpose different settings were tried, changing some fundamental registers responsible for the threshold like those listed and explained on page 26.

Then several tests have been run under controlled conditions:

- one healthy(good) pixel was injected;

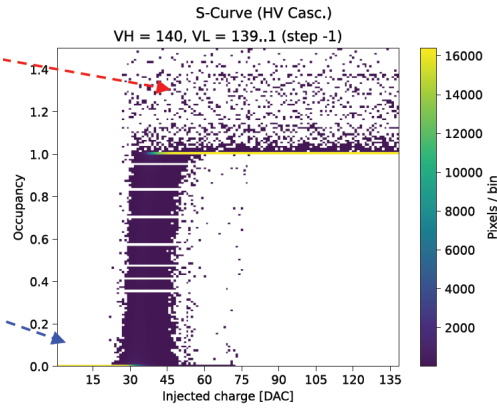


Figure 1.34: HV-Cascode s-curves.

- one *hot pixel* (two or three in different tests) was enabled but not injected;
- the all matrix except these pixels was disabled.

In this way (remembering the readout sequence [REFERENCE]) the readout cycle has a known duration and two different timing info has been used to study the induced signal with greater precision:

- $\Delta TS$  (TimeStamp) between two consecutive hits: the TimeStamp is assigned from the FPGA when the TOKEN rises on the TE of the first hit to read, but only if the previous readout frame is completed. So, if the hit coming from a *hot pixel* is after the hit from the injected one, the minimum  $\Delta TS$  has to be equal to the readout time of 1 pixel and so to the duration of the FREEZE\_STOP signal .

This info has allowed to verify if the hot pixel fires after the good injected one or not.

- LE(hit) - TE(previous hit): this quantity measures the elapsed time between a hit and the previous one. This is a finer info than the  $\Delta TS$  because it allows to correlate the hit with the induced digital signal, originate from the readout cycle.

Moreover, since a 7-bit BCID is sent to the matrix during its activity, it was important to keep short (<128 clock cycle) the duration of the full readout sequence and to not enable too many pixels in order to not extend too much the readout frame. Otherwise the information on the leading edge of the pixel could not be correlated with the token of the previous hit. In other words, if the readout frame exceed 128 clock cycles, since the token could be raised if the matrix is **not** freeze, even if an hit is arrived before it could be read only in the next frame when it could rise again the token, but in this case it will have different TimeStamp. So in this case the TS is useless for our purpose.

### 1.6.3 Cross-talk (Results)

Referring to the readout sequence, in order to understand which signal could induce cross talk, each register value has been moved one by one. In table on the next page just an example from the several settings tried is reported.

Register	Value
FREEZE_START_CONF	10
READ_START_CONF	13
READ_STOP_CONF	15
LOAD_CONF	30
FREEZE_STOP_CONF	31
STOP_CONF	31

Table 1.6: Register values of the Readout cycle.

Doing so indeed, the LE-TE info has to shift by the same value with which the signal that cause the cross talk has been changed. This step of the procedure is tied with the necessity to keep the readout sequence within the maximum 128 BCID range.

For example, if FREEZE\_START\_CONF is responsible for the cross talk signal, we expect that shifting its value by a certain amount, the hot pixels start to fire after that this signal arises due to the hit on the injected pixel. So the value of LE-TE has to be FREEZE\_START\_CONF + some potential delay. Same argument for the other registers.

By this procedure, repeated for each readout register, we have come to the conclusion that the cross-talk could be related to the raising and falling edge of the FREEZE signal.

In figure on the following page an example of some results obtained. It is the histogram of the time last between the leading edge of an hit and the trailing edge of the previous hit, when one pixel is injected and two are read. It's possible to see several peaks (referring to the readout setting reported in table on the current page):

- one at 0, that represent the situation in which both hits come from hot pixel firing simultaneously after the injection. This means that they are activated by the same signal and so it is the most important confirmation that is cross-talk and not random firing pixel signal;
- one at  $\approx 18$  equal to FREEZE STAR raising + 8  $\rightarrow$  first induced signal;
- one at  $\approx 35$  equal to FREEZE STOP falling + 4  $\rightarrow$  second induced signal;
- one at  $\approx 55$  equal to FREEZE STOP falling + 4 when two different pixels are read. In more details, after the first 30 time unit until the first LOAD CONF, a distinct pixel reading starts and it takes another 20 time unit (LOAD - FREEZE START) + 1 unit time to conclude the frame with the FREEZE STOP and so 51 + 4 unit time wrote above. Therefore when two pixels are read, the FREEZE STOP falls after 51 clock cycles, and it is compatible with the last peak in the plot.

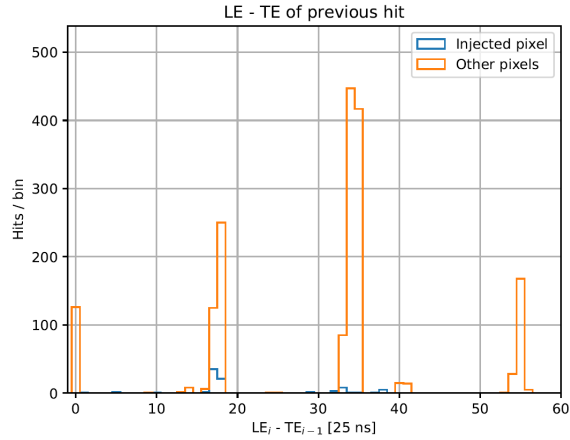
As already stated, we run several tests varying the number of pixels to read, the value of the readout registers, different combination of hot and good pixels and also different spatial location of them in the matrix to exclude the possibility that the problem was related to particular columns. All results are in agreement with the interpretation explained above.

?????...

Furthermore it has been tried to estimate the height of the induced signal from the threshold of the hot pixel. For this reason we have tried different setting of the currents cited above to make a pixel *hot* in order to understand when the induced signal went above the threshold.

Injected pixel: (217, 140)						
Other pixels: [(218, 155) (222, 188)]						
Assuming timestamp clock = 40.00 MHz						
Green = injected pixels						
Row	Col	LE	TE	$\Delta LE$	$\Delta TE$	$\Delta TS[25ns]$
140	217	12	29	124	123	5627.0000 635972.0000
140	217	8	25	124	124	5628.0000 641600.0000
155	218	60	60	52	35	35.0000 641635.0000
188	222	59	60	127	0	0.0000 641635.0000
155	218	115	115	56	55	55.0000 641690.0000
188	222	114	115	127	0	0.0000 641690.0000
155	218	42	43	56	56	55.0000 641745.0000
188	222	42	42	0	127	0.0000 641745.0000
140	217	4	21	90	107	5482.0000 647227.0000

(a) An example of the time quantity used in the analysis.



(b) An example of the LE(hit)-TE(previous hit) histogram.

Figure 1.35: Some results of the cross-talk studies.

We have found that the signal could (may) correspond to 100/150  $e^-$ .  
???????

In figure on the following page an analog acquistion of the readout signals taken by an oscilloscope.

In these tests one pixel was injected from 0 to 140 DAC (in the acquisition it can be seen in the increasing signal height). There are two different group of spikes: the first which is smaller and represent the cross-talk from the raising of the FREEZE signal and the second, larger and corresponding to the cross talk from the falling edge of the same signal. Moreover it's possible to see that in the two different pictures, the cross talk signals move according to the different settings of the FREEZE START/STOP edge.

#### 1.6.4 Mitigation

As seen in the previous, the problem of the hot pixel is tied to the induction signal produced during the readout, which cause cross-talk. It becomes even more serious when there is a grater dispersion threshold.

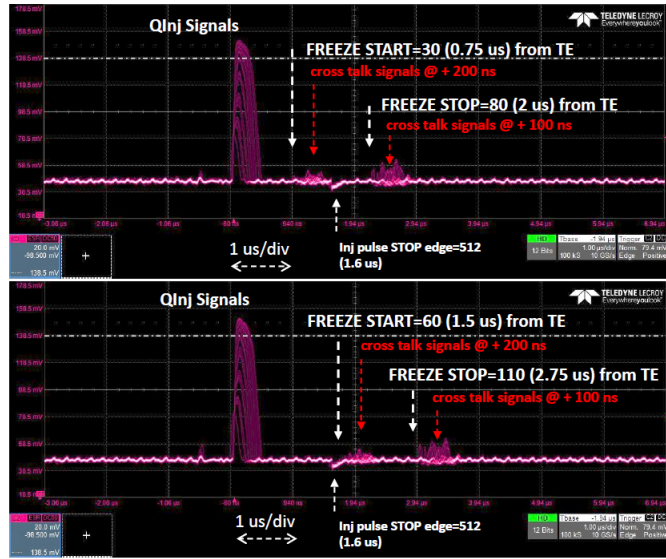


Figure 1.36: Cross-talk of the FREEZE signal on oscilloscope's analog output, for different value of FREEZE\_START\_CONF register.

Potentially every pixel could become *hot* if its threshold is lower than the height of the cross-talk signal, since the FREEZE is sent across the entire matrix.

As an example, in figure on the next page it is possible to compare the behaviour of pixel (218, 123) for different register settings adopted in order to reduce the threshold.

### Threshold trimming

Therefore a possible treatment could be related to the threshold tuning, explained in section (?? on page ??), which could allow to make the pixel threshold more uniform (less threshold dispersion) and simultaneously to target a value greater than the induced signals.

In figure on page 37 an example of the results obtained.

It's evident the reduction of the tail in the threshold distribution, in fact the dispersion is reduced by 56%. Also the hot pixels decrease from 18% to 1.2% of the total number of pixels studied. We can also notice that the peak at 0 threshold disappears.

### Bias Voltage

Moreover it has been tried to increase the voltage bias of the all matrix, too. We remember that all previous test has been run with  $P_{WELL}/P_{SUB}$  set to -3 V. This value was increased to -6 V and indeed there were some improvements. In fact increasing the bias, we expected a decrease of the diode capacitance thus higher gain and lower threshold dispersion. In addition the coupling with the cross talk signal is reduced too and so the induced signal height.

In figure on page 37 a comparison between the threshold distribution respectively at -3 V and -6 V, with same registers setting and without tuning.

At higher bias voltage not only is the threshold lower (higher gain), but also its dispersion, as expected. And despite that there are fewer hot pixels: 1.3% at -6V against 17% at -3 V. Also here there is clear a reduction of the threshold distribution tail.

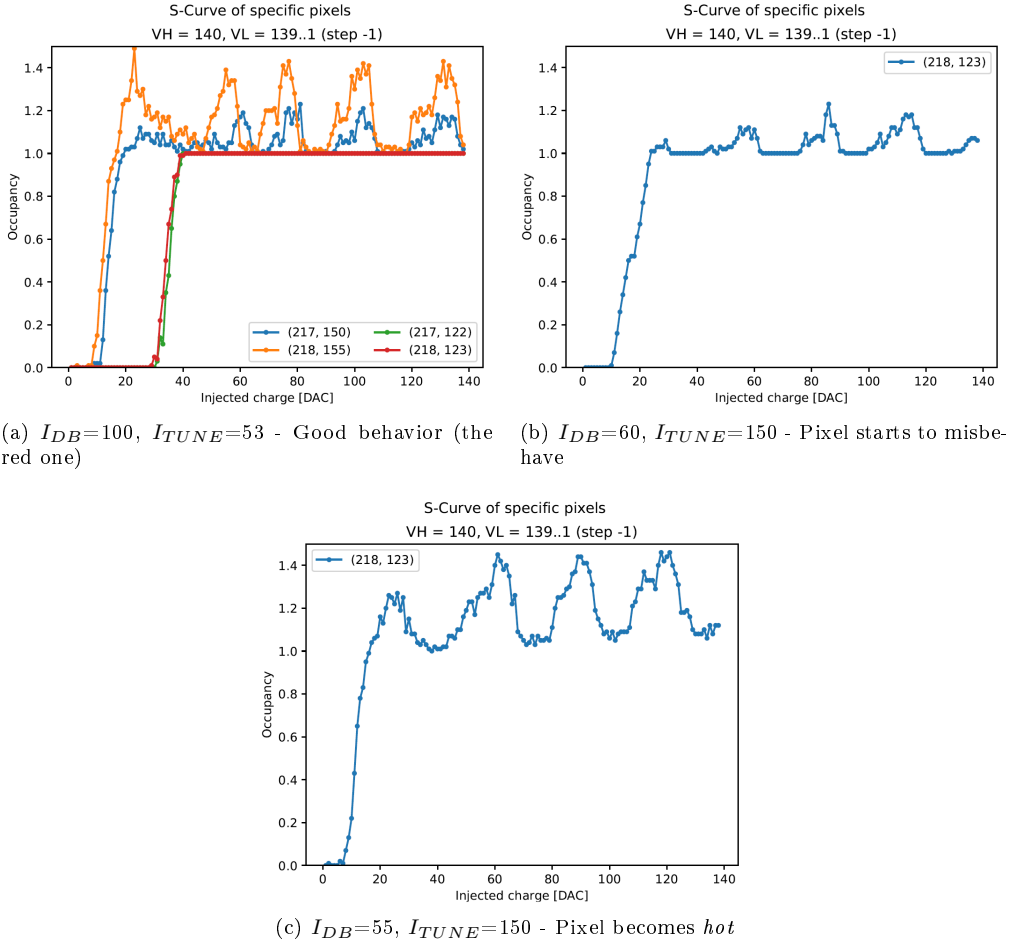


Figure 1.37: S-curve of the pixel (218, 123) for different register settings.

#### 1.6.4.1 Final results?

Eventually the final results obtained with both threshold tuning and a bias voltage on  $P_{WELL}/P_{SUB} = -6$  V.

As we can see in figure on the next page, the threshold dispersion decreases together with the number of the hot pixels. In fact without the tuning, there are 1.3% of them, instead with tuning procedure there are none at all.

## 1.7 Test Beam results

This full characterization of the chip allowed to interpret data collected during the Test Beam done in Desy in June 2022. Several measurements have been taken, among which: pixel response, noise level, cluster signal, full depletion depth, voltage scan and angular scan. In particular the aim was to study electrical characteristics and hit detection efficiency of unirradiated modules.

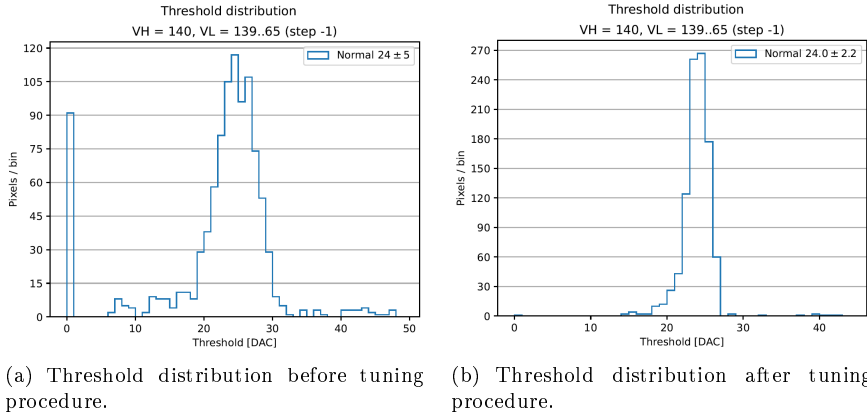
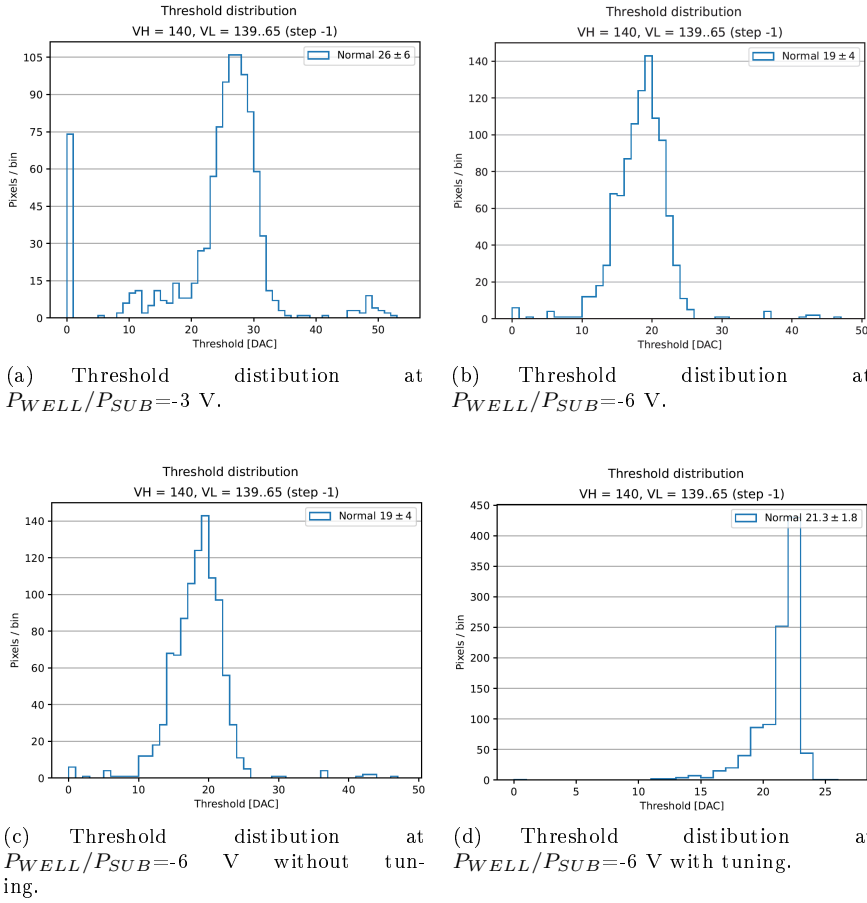


Figure 1.38: Threshold tuning to reduce hot pixels.



### 1.7.1 Experimental apparatus and DUTs

The measurements have been performed in a 4 (or 5) GeV electron beam at DESY II testbeam facility at DESY, Hamburg. The experimental apparatus consisted of a beam telescope, a Trigger

Logic Unit to provide trigger and control signals employed during test beams, a scintillator trigger and a rotation-translation stage on which install the device under test. (figure on this page).

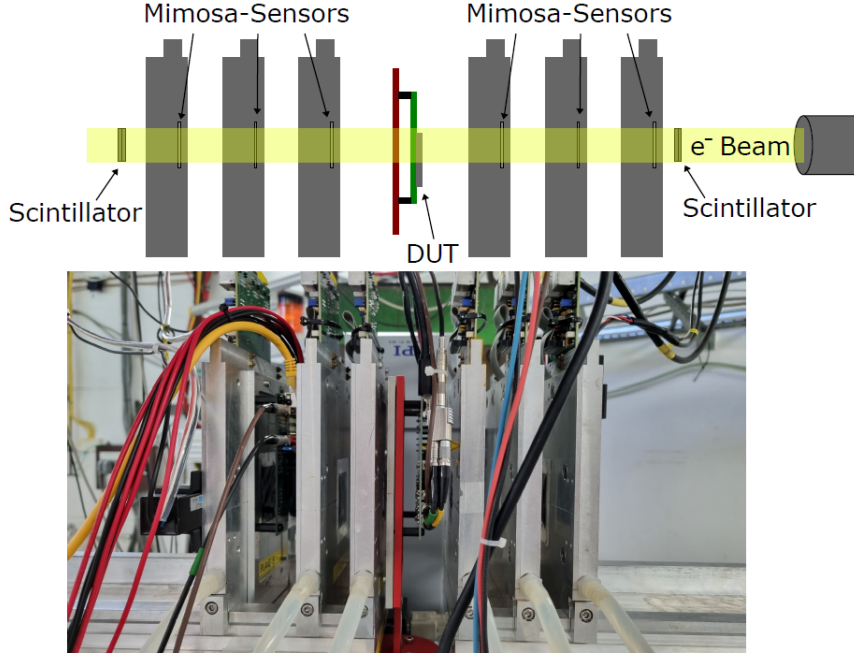


Figure 1.39: Test Beam experimental apparatus.

Three different modules have been tested with different sensor geometry, among which the chip W14R12 that we have studied in depth through laboratory measurements. All results described in previous sections have been crucial to interpret data obtained during these tests.

In the following we will briefly mention the results obtained.

### 1.7.2 Hit detection efficiency measurements

Initially a depletion depth study have been done and with a voltage bias of -3 V (Normal and Cascode FE), for the chip W14R12 resulted  $33\mu\text{m} \pm 0.04$  (stat.)  $\pm 2.53$  (sys.).

Voltage scan measurements have been performed for both the two type of pixel couplings, such as DC and AC coupled. For the latter, only some first results have been obtained.

#### Normal FE

In figure on the next page are reported results obtained for **Normal FE** of all modules. As expected, efficiency and clusters grow as the bias voltage is increased.

#### Cascode FE

Same trends for **Cascode FE** are shown in figure on the following page.

In particular in figure on the next page are reported the hit map efficiency for DC-coupled pixels for the W14R12 chip, which includes Normal and Cascode FE.

#### HV Casc. FE

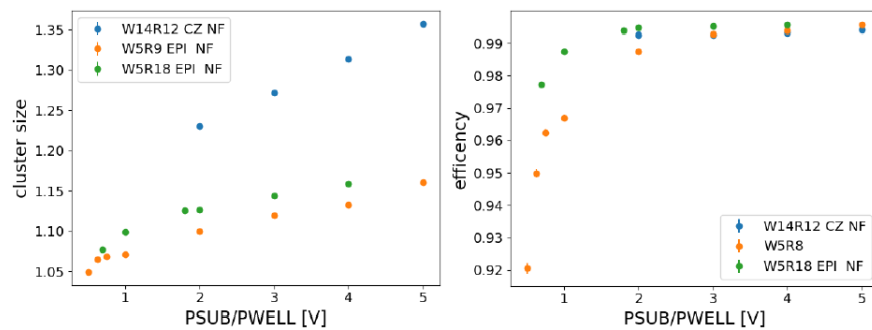


Figure 1.40: Cluster size and efficiency results for Normal FE.

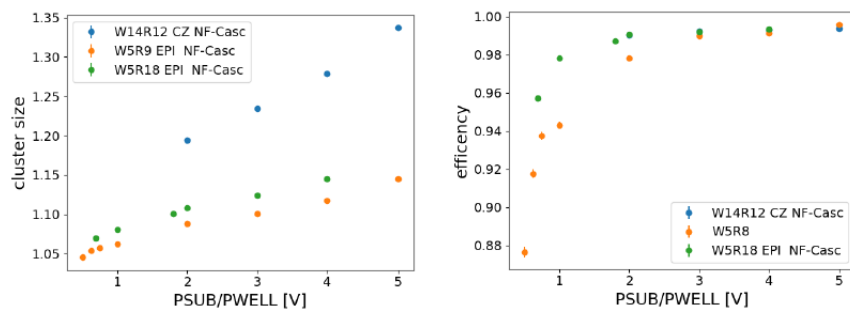


Figure 1.41: Cluster size and efficiency results for Cascode FE.

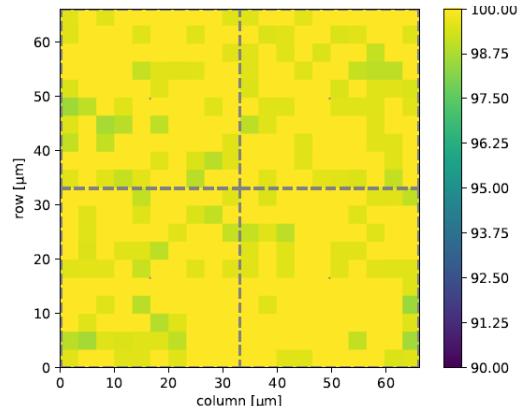


Figure 1.42: Efficiency for DC-coupled pixel of W14R12 chip:  $(99.79 \pm 0.10)$  %

## HV FE

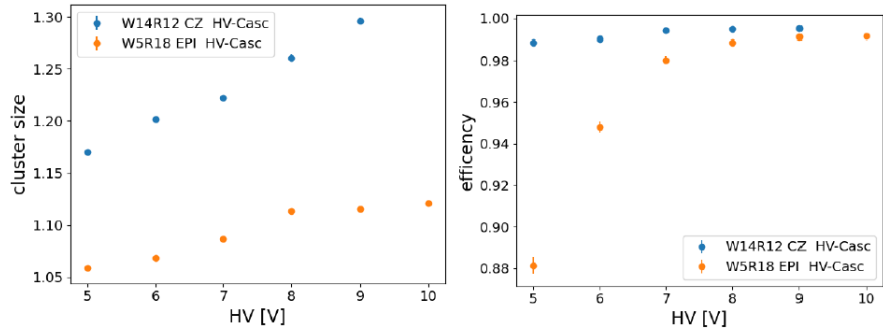


Figure 1.43: Cluster size and efficiency results for HV Cascode FE.

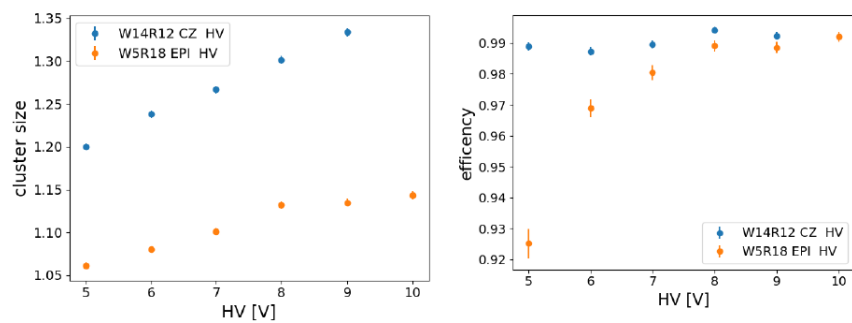


Figure 1.44: Cluster size and efficiency results for HV FE.

## 2. Conclusions